A Modeling Study of the Three-Dimensional Continental Shelf Circulation off Oregon. Part I: Model–Data Comparisons

PETER R. OKE,* J. S. ALLEN, R. N. MILLER, G. D. EGBERT, J. A. AUSTIN, J. A. BARTH, T. J. BOYD, P. M. KOSRO, AND M. D. LEVINE

College of Oceanic and Atmospheric Sciences, Oregon State University, Corvallis, Oregon

(Manuscript received 9 May 2001, in final form 19 September 2001)

ABSTRACT

Sixty-day simulations of the subinertial continental shelf circulation off Oregon are performed for a hindcast study of summer 1999. Model results are compared with in situ currents, high-frequency radar–derived surface currents, and hydrographic measurements obtained from an array of moored instruments and field surveys. The correlations between observed and modeled alongshore currents and temperatures in water depths of 50 m are in excess of 0.8. A study designed to test the model's sensitivity to different initial stratification, surface forcing, domain size, and river forcing demonstrates that surface heating is important, and that the model results are sensitive to initial stratification. An objective criterion for assessing the skill of a model simulation relative to a control simulation is outlined, providing an objective means for identifying the best model simulation. The model–data comparisons demonstrate that temperature fluctuations off Newport are primarily in response to surface heating and that subsurface density fluctuations are controlled by the wind-forced circulation through salinity. Experiments with river forcing indicate that, in the vicinity of Newport, the Columbia River plume is typically greater than 15 km from the coast and is confined to the top few meters of the water column. Additionally, the model–data comparisons suggest that the strongest upwelling occurs to the north of Newport where the continental shelf is relatively narrow and uniform in the alongshore direction. Part II of this study investigates the modeled three-dimensional circulation and dynamical balances.

1. Introduction

A numerical modeling study of the coastal ocean circulation off Oregon during the 1999 upwelling season is presented. The model results are compared with in situ velocity, temperature and salinity measurements, and high-frequency (HF) radar–derived surface currents obtained during summer 1999 as a part of the Oregon State University (OSU) National Oceanographic Partnership Program (NOPP) project.

The aims of this study are to assess the performance of the model, to identify the dominant physical processes, and to assess the model's sensitivity to variations in initial stratification, surface forcing, model domain size, and river forcing. Processes that are of particular interest in this study include the response to wind forcing and the generation of the northward flow that is commonly observed off Newport (44.65°N) over the innershelf after strong upwelling events. The performance of each experiment is objectively assessed by calculating a skill score (e.g., Murphy 1992) relative to a basic test case, based on the model's mean-square error (MSE) at the observation locations.

The outline of this paper is as follows. Details of the observational program are presented in section 2, followed by a description of the model configuration in section 3, the numerical experiments in section 4, a series of model–data comparisons in section 5, and a summary in section 6. The details of the surface heat flux formulation, river input, an analysis of the MSE, and the details of the sensitivity study are presented in appendices A, B, C, and D, respectively.

2. Observational program

The period of interest for this study is between 18 June 1999 and 17 August 1999. Time series of the observed wind stress τ^S, where the alongshore direction is taken to be 7°N, and surface heat flux Q in the vicinity of Newport are plotted in Fig. 1. Observations collected during the 1999 OSU NOPP field season (denoted in Fig. 1) include time series of across-shore velocity u, alongshore velocity v, and temperature θ, from an inshore (IS: water depth 50 m) and midshelf (MS: water

* Current affiliation: School of Mathematics, University of New South Wales, Sydney, New South Wales, Australia.

Corresponding author address: Dr. Peter R. Oke, School of Mathematics, University of New South Wales, Sydney, NSW 2052, Australia.
E-mail: petero@maths.unsw .edu.au

© 2002 American Meteorological Society

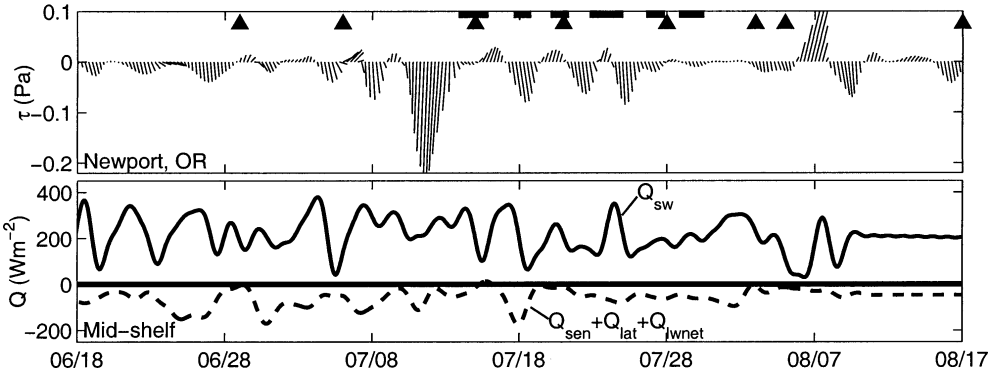

FIG. 1. Observed wind stress τ^s from Newport (top) and surface heat flux Q from the MS mooring (bottom) for summer 1999. The time of each MiniBAT and SeaSoar survey is denoted by a triangle and a thick line, respectively, on the top of the upper panel.

depth 80 m) mooring (Figs. 2 and 3; Boyd et al. 2000). Low-pass filtered measurements of u, v, and θ from the IS and MS moorings are compared with modeled variables for the experiments described in section 4. A meteorological station on a buoy adjacent to the MS mooring provides measurements of air temperature, relative humidity, shortwave radiation, and wind speed, enabling a time series of Q to be estimated (Fig. 1, appendix A).

In addition to the moored observations, eight high-resolution ($\Delta x \approx 1$–2 km, $\Delta z < 1$ m) hydrographic surveys of θ and salinity S were made during the field season (denoted in Fig. 1) using a Guildline MiniBAT vehicle equipped with an SBE-25 conductivity–temperature–depth (CTD) instrument (Austin et al. 2000). These surveys were performed from the R/V *Sacajawea* along the Newport Hydrographic line (44.65°N) denoted in Figs. 2 and 3, between the coast and the 100-m isobath (≈30 km offshore). The MiniBAT θ and S fields are objectively analyzed for vertical bins that are separated

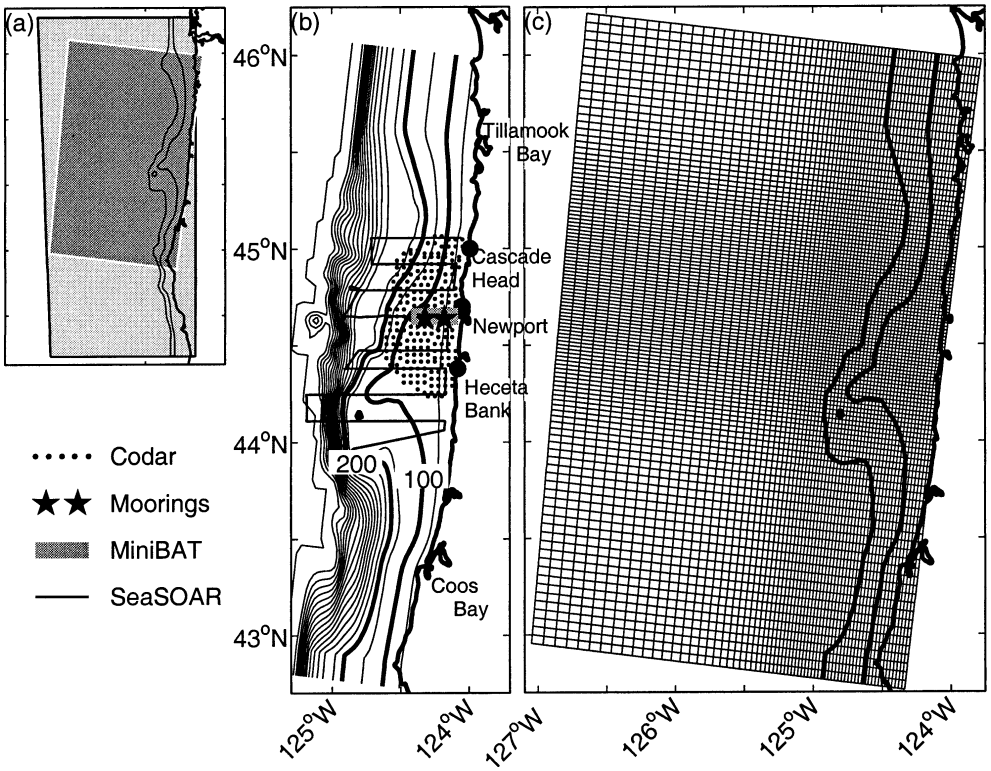

FIG. 2. (a) Outline of the standard (dark) and extended (light) model domains; (b) the model topography (contour interval = 50 m; the 100 and 200 m isobaths are bold) for the standard domain showing the mooring locations, MiniBAT sections, SeaSoar surveys, and CODAR locations; and (c) the standard model grid.

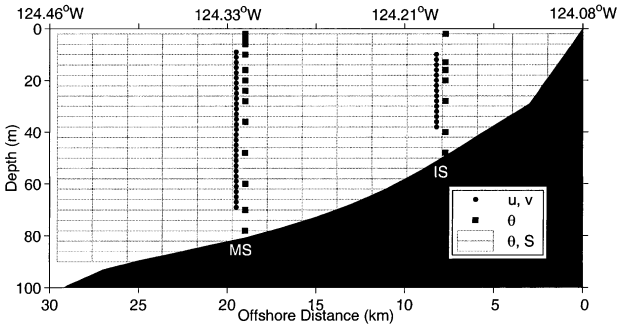

FIG. 3. Schematic diagram of the mooring array (IS: Inshore; MS: Mid-shelf) and the grid onto which the MiniBAT θ and S are objectively analyzed.

vertically by 4 m onto the grid shown in Fig. 3 (Δx = 2 km, Δz = 4 m) using a horizontal decorrelation length scale of 4 km after Austin et al. (2000).

Several large-scale hydrographic surveys were also performed during the field season off the R/V *Wecoma* using a profiling SeaSoar CTD (Barth et al. 2001). These surveys provide maps of θ and S with greater spatial coverage (between the 50- and 300-m isobath; 44.1–45.2°N), but more limited temporal coverage (Fig. 1) compared to the MiniBAT surveys. Time series of surface currents for a region between approximately 44.2° and 45.1°N, from the coast out to about the 200-m isobath were also obtained from a land-based HF radar system (CODAR; e.g., Kosro et al. 1997; Fig. 2).

The observational program outlined above provides an excellent, yet necessarily incomplete picture of the three-dimensional continental shelf circulation off Oregon. By configuring a numerical model for the above-mentioned period, a more detailed description of the three-dimensional, time-varying circulation is obtained, together with information concerning the dominant dynamical balances. The fields and dynamical balances are analyzed in detail in Part II of this study (Oke et al. 2002a).

3. Model configuration

For an in-depth description of the Princeton Ocean Model (POM) that is utilized here the reader is referred to Blumberg and Mellor (1987). The standard model configuration is the same as that utilized by Oke et al. (2002b) for a coastal data assimilation study of the upwelling circulation off Oregon for summer 1998. The standard model grid (Fig. 2) extends 220 km offshore and 365 km in the alongshore direction. The extended domain model (EDM; Fig. 2) extends 260 km offshore and 575 km in the alongshore direction. For both model grids the maximum horizontal grid resolution is 2 km over the shelf in the vicinity of Newport, with decreased resolution toward the offshore and alongshore boundaries. The grid is rectangular and the axes have been rotated to 7°N in order to better align with the coastline. The horizontal velocity **v** has components (u, v) corresponding to the across-shore and alongshore velocities [depth-averages denoted by **V** and (U, V)] in the (x, y) directions, so that u is positive onshore and v is positive toward the north. The vertical grid consists of 31 sigma-levels, with 8 levels concentrated near the surface, and 4 near the bottom in order to resolve the respective boundary layers.

The model topography (Fig. 2) is linearly interpolated from a 1-km resolution dataset and smoothed to reduce the effects of pressure gradient errors due to the sigma coordinates. The minimum depth is 10 m. The maximum depth is set to 1000 m in order to reduce the constraint on the time steps that are 6 and 180 s for the barotropic and baroclinic modes, respectively. The vertical and horizontal viscosity (and diffusion) coefficients are flow-dependent according to the level-2.5 turbulence closure model of Mellor and Yamada (1982) and the formulation of Smagorinsky (1963), respectively. The horizontal diffusion coefficients are small (typically <10 m^2 s^{-1}) throughout each experiment considered in this study.

The alongshore boundary conditions are periodic for all variables. Consistent with this condition, an f-plane approximation is used, with $f = 1.037 \times 10^{-4}$ s^{-1}. In addition, an across-shore topographic section near the southern extent of the domain is interpolated over 10 alongshore grid cells to match an across-shore section near the northern extent of the domain, so that the topography is periodic in the y direction. The use of periodic boundary conditions establishes a well-posed and robust model, but is a limiting feature of this configuration. The most limiting aspect of this configuration is the model's inability to represent net alongshore pressure gradients that might result from large-scale, alongshore density gradients for example. Additionally, periodic boundary conditions force the modeled flow at the northern and southern extent of the domain to be equal. Clearly this is inconsistent with conditions in the real ocean. With these limitations noted, we find that this configuration is capable of reproducing a substantial fraction of the observed variance of the horizontal velocity fields in the region of interest.

The offshore boundary conditions are zero gradient for the tangential velocities and elevation η, a modified radiation condition for the normal velocities (e.g., Chapman 1985), and an upstream advection condition for the θ and S. The horizontal diffusion coefficient is increased smoothly over five grid cells adjacent to the offshore boundary to a maximum of 1000 m^2 s^{-1} at the boundary in order to damp out unwanted reflection. The alongshore component of the applied wind stress τ^{Sy} is calculated from time-varying winds measured at Newport and is assumed to be spatially uniform for most of the experiments. To reduce the excitation of inertial oscillations, the wind is low-pass filtered with a 40-h half-amplitude filter. The applied surface heat flux Q is calculated from meteorological observations as discussed in section 2 and appendix A. The shortwave component,

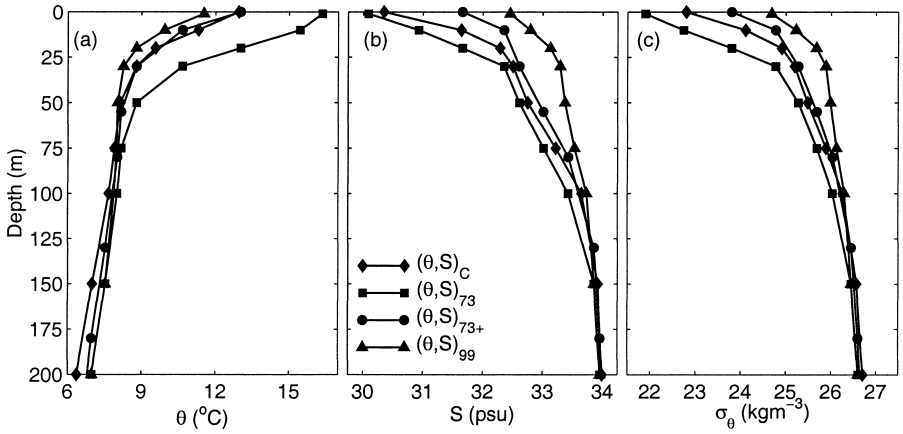

FIG. 4. (a) Temperature θ, (b) salinity S, and (c) potential density σ_θ for the June climatology (1961–71) off Newport at approximately 50 km offshore $(\theta, S)_C$; 1973 average $(\theta, S)_{73}$; 1973 average with the pycnocline raised by 20 m $(\theta, S)_{73+}$; the 1999 shelf average (calculated from the SeaSoar CTD surveys) $(\theta, S)_{99}$.

Q_{sw}, of the total Q is spatially uniform, while the contributions from the net longwave, sensible, and latent heat fluxes (Q_{lwnet}, Q_{sen}, and Q_{lat}, respectively), vary in space, depending on the difference between the observed air temperature at the MS mooring location and the modeled ocean surface temperature.

Numerical experiments are performed with four different hydrographic profiles (Fig. 4): the mean observed profile during June between 1961 and 1971 at a station approximately 50 km offshore of Newport (Smith et al. 2001) denoted as $(\theta, S)_C$; the mean observed profile at that offshore station during the 1973 coastal upwelling experiment (CUE-II) denoted as $(\theta, S)_{73}$; the profile $(\theta, S)_{73}$ with the pycnocline raised by 20 m denoted as $(\theta, S)_{73+}$; and, for the upper 150 m of the water column, the spatially averaged observed θ and S at each depth from the SeaSoar CTD surveys conducted during the 1999 observational program denoted as $(\theta, S)_{99}$. The initial fields of θ and S are horizontally uniform and the initial velocity fields are zero. The motivation for the $(\theta, S)_{73+}$ profile is to reduce the bias in θ that results when initializing with $(\theta, S)_{73}$ and to raise the depth of the initial pycnocline to be in better agreement with offshore profiles from the SeaSoar CTD surveys.

For each experiment the model fields are spun up over 10 days with 5 days of constant 0.1 Pa, upwelling favorable winds followed by 5 days of no wind. This spinup allows the pycnocline to be upwelled to the surface and then relax to a quasi-equilibrium position. The fields of v after the spin up period are characterized by a baroclinic southward coastal jet with maximum current magnitudes of approximately 0.4 m s^{-1} located over the 80 m isobath, and a weak northward flow ($v \approx 0.1$ m s^{-1}) over the innershelf off Newport and Heceta Bank. The fields of σ_θ after the spinup period are characterized by isopycnals that are uplifted over the shelf and generally tilt upward toward the coast.

TABLE 1. Summary of experiments. Subscripts of (θ, S) refer to different initial hydrographic profiles (section 3); τ^{Sy} and $\tau^{Sy}(x)$ refer to spatially uniform and spatially varying wind stress, respectively; τ^{Sx} refers to across-shore wind stress; Q_{III} and Q_{Obs} refer to surface heating with water type III and the observed water type, respectively; River refers to idealized river forcing and EDM indicates that an extended domain is utilized.

Expt	Initial conditions	Surface forcing	Additional features
1	$(\theta, S)_{73}$	τ^{Sy}	—
2	$(\theta, S)_{73}$	τ^{Sy}, Q_{III}	—
3	$(\theta, S)_{73}$	τ^{Sy}, Q_{Obs}	—
4	$(\theta, S)_{73+}$	τ^{Sy}	—
5	$(\theta, S)_{73+}$	τ^{Sy}, Q_{III}	—
6	$(\theta, S)_{73+}$	τ^{Sy}, Q_{Obs}	—
7	$(\theta, S)_{99}$	τ^{Sy}	—
8	$(\theta, S)_{99}$	τ^{Sy}, Q_{III}	—
9	$(\theta, S)_{99}$	τ^{Sy}, Q_{Obs}	—
10	$(\theta, S)_C$	τ^{Sy}	—
11	$(\theta, S)_C$	τ^{Sy}, Q_{III}	—
12	$(\theta, S)_C$	τ^{Sy}, Q_{Obs}	—
13	$(\theta, S)_{73+}$	$\tau^{Sy}(x)$, Q_{III}	—
14	$(\theta, S)_{73+}$	$\tau^{Sy}(x)$, Q_{Obs}	—
15	$(\theta, S)_{73+}$	τ^{Sy}, τ^{Sx}, Q_{Obs}	—
16	$(\theta, S)_{73+}$	τ^{Sy},Q_{Obs}	River
17	$(\theta, S)_{73+}$	$\tau^{Sy}(x)$, Q_{Obs}	River
18	$(\theta, S)_{73+}$	τ^{Sy}	EDM
19	$(\theta, S)_{73+}$	τ^{Sy}, Q_{Obs}	EDM
20	$(\theta, S)_{73+}$	τ^{Sy}, τ^{Sx}, Q_{Obs}	EDM

4. Experiments

A series of numerical experiments are performed with different initial stratification, surface forcing, domain size, and river forcing. The details of the experiments are summarized in Table 1. For every experiment, time-varying winds observed at Newport between 18 June and 17 August during 1999 are applied (Fig. 1) following the 10-day model spinup. During this period there is a strong upwelling favorable wind event on 12 July,

hereafter the 12 July upwelling, followed by a two-week period of weak oscillatory winds. This time period corresponds to the intensive OSU NOPP field observations outlined in section 2 and Fig. 1. Prior to the 12 July upwelling, the winds are weak and mostly upwelling favorable. Following 28 July, the winds are near zero for 10 days, before a short, moderate downwelling favorable wind pulse on 7 August. The mean τ^{Sy} at Newport during the period of interest is -0.017 Pa with a standard deviation of 0.044. For historical context, the mean τ^{Sy} for the same period in 1973, during CUE-II (Kundu and Allen 1976) was -0.019 Pa with a standard deviation of 0.032 Pa and during 1998 (Oke et al. 2002b) was -0.0084 Pa with a standard deviation of 0.026 Pa. For many of the experiments, surface heating is also applied (Table 1). The average observed heat flux at the MS mooring is 144 W m^{-2} with a standard deviation of 69 W m^{-2}.

The model's sensitivity to the initial stratification is assessed by initializing with four different profiles of θ and S as outlined in section 3 and Fig. 4. The importance of surface heating is assessed by running experiments without heating (expts 1, 4, 7, 10 and 18) and with heating (expts 2–3, 5–6, 8–9, 11–12, and 19). The importance of surface heating off the Oregon coast has previously been demonstrated by Federiuk and Allen (1995) using an idealized two-dimensional model. The standard coastal water type is type III, which has an *e*-folding attenuation scale for Q_{sw} of approximately 8 m. The observed *e*-folding attenuation scale, estimated from observations of transmission from the MiniBAT surveys (Austin et al. 2000), is approximately 1.5 m. Experiments are performed with the attenuation scale of type III water denoted by Q_{III}, and with the observed attenuation scale denoted by Q_{Obs}, in order to test the model's sensitivity to this parameter (expts 2–3, 5–6, 8–9, 11–12, 13–14).

A first-order assessment of the effects of spatially varying winds is made by running experiments with spatially uniform winds (expts 5, 6, 16) and with winds that increase in the offshore direction (expts 13, 14, 17). For the experiments with spatially varying τ^{Sy}, denoted by $\tau^{Sy}(x)$, the observed winds at Newport are multiplied by an amplitude function that increases from 1 at the coast, to a maximum of 1.75 near the offshore boundary with a structure that varies like $\tau^{Sy}(x) \approx (1 + x^{0.5}/20)\tau^{Sy}$, where x is the distance, in kilometers, from the coast. The amplitude function is the alongshore average of the first EOF, representing approximately 78% of the total variance, of the modeled wind stress from a three-month, high-resolution simulation of the coastal atmosphere (Samelson et al. 2002).

Experiments are also performed in order to assess the model's sensitivity to domain size. For a limited number of experiments an EDM that extends from 41.4° to 46.8°N is utilized (expts 18–20). In contrast, the standard domain extends from 42.7° to 46.2°N. The effects of including a constant freshwater source from the Columbia River is investigated by comparing experiments with and without river forcing (expts 6, 16 and 14, 17). The details of the river input are described in appendix B. Other sensitivity experiments investigate the effects of including the across-shore component of the wind stress τ^{Sx} (expts 15 and 20).

The control for this study is expt 1 with spatially uniform, time-varying winds; no surface heating; and no river input on the standard domain. This experiment is the reference to which all other experiments are compared in section 5.

5. Model–data comparisons

a. Defining model skill

As described in section 4 a series of numerical experiments are performed (Table 1). In order to determine which experiment performs the best, the modeled and observed fields at the IS and MS moorings are compared. The ith modeled and observed variable is denoted by m_i and o_i, respectively; $\overline{m}$ and $\overline{o}$ are the respective means; S_m and S_o are the respective standard deviations; and CC is the cross-correlation between the modeled and observed fields. The most commonly used measure of accuracy of a model forecast in numerical weather prediction (e.g., Murphy 1992) that is adopted here is the MSE:

$$\mathrm{MSE} = \frac{1}{n}\sum_{i=1}^{n}(m_i - o_i)^2, \tag{5.1}$$

where n is the number of observed and modeled variables in time. The MSE can be written in terms of the model bias

$$\mathrm{MB} = \overline{m} - \overline{o}, \tag{5.2}$$

the standard deviation error

$$\mathrm{SDE} = S_m - S_o, \tag{5.3}$$

and S_m, S_o, and CC (see appendix C for details):

$$\mathrm{MSE} = \mathrm{MB}^2 + \mathrm{SDE}^2 + 2S_mS_o(1 - \mathrm{CC}). \tag{5.4}$$

The skill of each experiment, with respect to a reference experiment (expt 1), is calculated based on the MSE. The skill score (SS; e.g., Murphy 1992) is defined as

$$\mathrm{SS} = 1 - \frac{\mathrm{MSE}}{\mathrm{MSE}_R} \tag{5.5}$$

where the subscript R denotes a reference experiment. As defined in (5.5), SS > 0 when MSE $<$ MSE$_R$ (positive skill), SS $= 0$ when MSE $=$ MSE$_R$ (no skill), SS < 0 when MSE $>$ MSE$_R$ (negative skill), and SS $= 1$ when MSE $= 0$ (perfect agreement with observations). The SS is a single number by which we can objectively determine which numerical experiment performs the best.

In order to fully assess the performance of each experiment, the depth averages of the normalized root-

TABLE 2. Average SS (5.5) for u, v, and θ from the IS and MS moorings and for θ and S from the MiniBAT surveys. The average over all variables from all measurements is presented. The highest SS in each column is highlighted in bold.

	IS mooring			MS mooring			MiniBAT		
Expt	u	v	θ	u	v	θ	θ	S	Average
1	0	0	0	0	0	0	0	0	0
2	0.19	0.18	−1.23	0.01	0.05	−1.05	−1.50	−0.08	−0.43
3	0.09	0.15	−0.86	−0.14	−0.08	−0.73	−1.20	−0.08	−0.36
4	0.30	0.19	−0.35	−0.05	0.26	−0.28	−0.28	0.19	0
5	0.32	0.37	0.16	−0.06	0.17	0.56	0.43	0.19	0.27
6	0.32	**0.38**	**0.36**	−0.08	0.21	0.62	0.47	0.23	**0.32**
7	0.13	0	−0.78	0.13	0.35	−0.55	−0.56	−0.3	−0.20
8	0.28	0	−0.07	**0.15**	0.32	0.37	0.51	−0.31	0.16
9	0.28	0	−0.07	**0.15**	0.32	0.37	0.51	−0.31	0.16
10	−0.10	−0.14	−0.97	0.07	0.15	−0.23	−0.37	0.35	−0.15
11	0.23	0.35	0.03	0.03	0.07	0.63	0.45	0.39	0.27
12	0.32	**0.38**	0.02	−0.05	−0.03	0.61	0.57	0.36	0.27
13	0.21	0.12	0.21	−0.06	0.16	0.68	0.60	0.12	0.26
14	0.21	0.19	0.05	−0.03	0.17	**0.69**	**0.63**	0.08	0.25
15	0.22	0.33	0.24	0.03	0.17	0.58	0.50	0.19	0.28
16	**0.35**	0.29	0.07	−0.01	0.22	0.28	0.38	0.06	0.21
17	0.22	0.28	−1.01	−0.15	0.19	0.67	0.55	**0.40**	0.14
18	0.09	0.12	−0.47	−0.12	**0.42**	−0.45	−0.47	0.19	−0.09
19	−0.06	0.18	0.16	−0.02	0.36	0.64	0.52	0.19	0.25
20	−0.03	0.21	0.17	−0.04	0.39	0.64	0.52	0.19	0.26

mean-squared error (RMSE), CC; the normalized MB; and the normalized SDE of u, v, and θ at the IS and MS moorings for each experiment are presented in appendix D. The RMSE, MB, and SDE are all normalized by S_o. The average rmse/S_o, CC, MB/S_o, and SDE/S_o over all variables are also presented in order to assess the overall performance of each experiment. The rms of MB/S_o and SDE/S_o are used in place of the average to provide an assessment of the magnitude of the normalized MB and SDE.

The average SS for u, v, and θ at the IS and MS moorings, and for θ and S from the MiniBAT surveys are presented in Table 2. The average SS over all variables from both the moorings and the MiniBAT surveys are also presented in Table 2 in order to quantify the relative skill of each experiment in a single number. The number of independent measurements of u, v, θ, and S are not equivalent in this average SS. In the absence of more observations, however, we proceed with this average in order to help identify the experiment with the most skill.

b. Model sensitivity

1) AVERAGE SKILL SCORES

The highest average SS from the moorings and the MiniBAT surveys is obtained from expt 6 (Table 2). The highest average SS from the MiniBAT surveys, the IS mooring and the MS mooring is obtained from expts 17, 6, and 20, respectively. Experiments 6 and 20 both utilize $(\theta, S)_{73+}$ initial stratification, spatially uniform τ^{Sy} and Q_{Obs} surface heating. Experiment 20 also utilizes τ^{Sx} and the EDM. Experiment 17 utilizes $(\theta, S)_{73+}$ initial stratification, $\tau^{Sy}(x)$, Q_{Obs}, and idealized river forcing. Other experiments that have notably high average SS are discussed below. Based on these statistical comparisons expt 6 is deemed to have the most skill. The modeled fields from expt 6 are analyzed in detail in Part II of this study.

2) COMPARISONS WITH MINIBAT SURVEYS

The mean and standard deviation of σ_θ for the MiniBAT surveys are presented in Figure 5 comparing observed and modeled fields from expts 4, 6, 14, 16, and 19 (Table 1), all of which utilize $(\theta, S)_{73+}$ initial stratification. For all of the experiments the mean position of the 26 σ_θ isopycnal is well represented. The most notable difference between the fields from the different model experiments is the near-surface σ_θ at greater than 15 km from the coast. All of the model experiments underestimate the near-surface standard deviation. The standard deviation of σ_θ is closest to the observed standard deviations of σ_θ when idealized river forcing and surface heating are applied (expt 16). This experiment shows that the Columbia River plume is located greater than 15 km from the coast and is confined to the top few meters of the water column. These characteristics are consistent with historical observations (e.g., Huyer 1983). Clearly expt 6, with surface heating, performs better than expt 4, with no surface heating, in both the mean and standard deviation. From these comparisons there is no obvious benefit in using $\tau^{Sy}(x)$ (expt 14) or the EDM (expt 19) over spatially uniform wind and surface heating on the standard domain (expt 6).

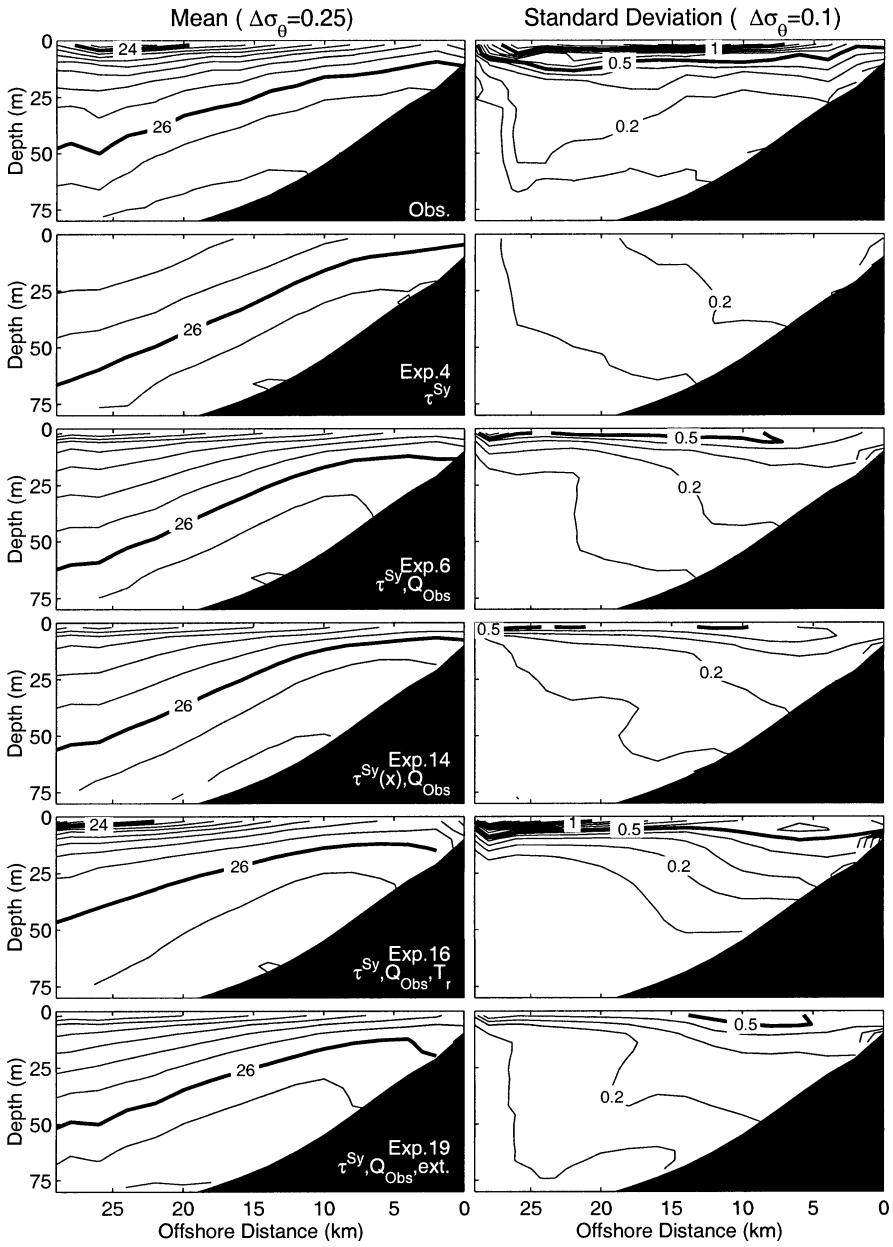

FIG. 5. Mean (left) and standard deviation (right) of σ_θ from the MiniBAT surveys (top), expts 4, 6, 14, 16, and 19 (top–bottom) as labeled, showing the importance of surface heating (compare expts 4 and 6) and Columbia River forcing (compare expts 6 and 16). The contour intervals are 0.25 and 0.1 for the mean and standard deviations, respectively.

3) SUMMARY OF SENSITIVITY STATISTICS

A complete description of the statistics of the sensitivity study are presented in appendix D. Briefly, this study demonstrates that the effects of varying the extinction coefficient in the application of Q_{sw} are minimal. The effects of including τ^{Sx}, idealized river forcing, or utilizing the EDM on the modeled fields at the moorings are small. Utilizing $\tau^{Sy}(x)$ improves the modeled θ over the midshelf; however, it does not significantly improve other aspects of the modeled circulation at the moorings. It is likely that alongshore variations in the wind field are also important (e.g., Samelson et al. 2002; Gan and Allen 2002) and that the across-shore structure of τ^{Sy} varies in both space and time. Time-variability of the across-shore structure of τ^{Sy} was first demonstrated by Halpern (1976). Varying the initial stratification is found to have a significant effect on the model skill (Table 2), with the average SS ranging from approximately -0.4 (expts 2–3), 0.3 (expts 5–6), 0.16 (expts 8–9), and 0.27 (expts 11–12) for experiments with surface heating and different initial stratification.

Varying the initial stratification significantly effects

θ and v, particularly at the IS mooring (appendix D). Why does the initial stratification influence the CC, the MB (5.2), and the SDE (5.3) for v? One might expect that, during wind-driven upwelling the initial $\partial\rho/\partial z$, where ρ is density, is directly related to the modeled $\partial\rho/\partial x$ since upwelling is effective at advecting (through across-shore circulation) and distorting (through vertical mixing) the vertical density profile to form a horizontal density gradient, or upwelling front. For the geostrophic component of v, $\partial v/\partial z$ is proportional to $\partial\rho/\partial x$ by the thermal wind relation

$$\frac{\partial v}{\partial z} = -\frac{g}{f\rho_0}\frac{\partial \rho}{\partial x}, \tag{5.6}$$

where g is gravity, f is the Coriolis parameter, and ρ_0 is a reference density. This simple argument demonstrates why the initial $\partial\rho/\partial z$, by affecting $\partial\rho/\partial x$, ultimately influences CC, the MB (5.2), and the SDE (5.3) of v. Why does varying the initial stratification have a greater effect at the IS mooring compared to the MS mooring? The IS mooring is in the region of the shelf where the upwelling front, the strong $\partial\rho/\partial x$, is typically located. Thus, the effects of varying $\partial\rho/\partial z$ are most evident in this region.

4) Currents at the IS mooring

Vector stick plots of observed and modeled (expt 6) currents at the IS mooring are presented in Fig. 6 showing the applied surface forcing, near-surface (12 m), middepth (20 m), and near-bottom (38 m) observed and modeled currents. There is generally excellent quantitative agreement between the observed and modeled currents at the IS mooring. The correlation between the modeled and observed (u, v), denoted as CC(u, v), and the magnitude and phase of the complex cross-correlation (Kundu 1976), denoted as (ρ^*, θ^*) is shown for each time series comparison. Near the surface CC(u, v) = (0.72, 0.87) and (ρ^*, θ^*) = (0.86, $-1.1°$). The agreement between the observed and modeled currents improves after the 12 July upwelling. For the 40-day period following 8 July, (ρ^*, θ^*) = (0.92, $-0.62°$), (0.9, $-6.4°$), and (0.83, $-6.9°$) at the near-surface, middepth and near-bottom depth on the IS mooring respectively demonstrating this point. Before the 12 July upwelling, the observed currents are oscillatory in the y direction with a period of 3–5 days. Similar variability is evident in the modeled fields; however, the period is longer and the amplitude is smaller. It is not clear whether the model is still spinning up during the period before 8 July, or whether the model does not adequately represent the dominant physical processes, such as remotely forced coastally trapped waves, that govern the circulation before 8 July.

During the 12 July upwelling the coastal jet accelerates, increasing the magnitude of v in excess of 0.5 m s^{-1} near the surface and 0.3–0.4 m s^{-1} near the bottom. After the 12 July upwelling, v reverses at all depths at the IS mooring. Close inspection reveals that the near-bottom currents reverse before the currents at middepth and near the surface in both the model and observations. Similar behavior was found by Gan and Allen (2002) in a modeling study of upwelling relaxation off northern California. For a two-week period after the 12 July upwelling the winds oscillate between being moderately upwelling favorable and weakly downwelling favorable. During this time, v oscillates approximately in phase with the wind. Immediately prior to 28 July there is a southward, vertically sheared pulse in v. Following this pulse, v reverses and flows northward. This reversal is very similar to the upwelling relaxation reversal that followed the 12 July upwelling. Again, it is clear that v reverses near the bottom first, before reversing at middepth and finally near the surface around 29 July. The main difference between this, and typical upwelling relaxation reversals is the absence of a single, strong upwelling favorable wind event immediately prior to the reversal. During the next 10 days the wind is near zero and v continues to flow northward. Around 7 August there is a brief downwelling event when v accelerates to the north. The dynamical balances that govern the reversal after the 12 July upwelling are investigated in detail in Part II of this study where it is shown that the northward momentum associated with this reversal is generated to the south of Newport by a negative alongshore pressure gradient and that the northward momentum is subsequently advected to the IS mooring location resulting in a sustained northward flow.

5) Currents at the MS mooring

Vector stick plots of observed and modeled (expt 6) currents at the MS mooring are presented in Fig. 7 showing the applied surface forcing, near-surface (11 m), middepth (41 m) and near-bottom (63 m) observed and modeled currents. There is generally good qualitative agreement between the observed and modeled fields. The best agreement is found to be near the bottom where CC(u, v) = (0.38, 0.59) and (ρ^*, θ^*) = (0.56, 10°). While the modeled and observed currents are qualitatively similar at the MS mooring the most striking difference is the MB (5.2) that develops after the 12 July upwelling. The observed currents accelerate to about 0.5ms $^{-1}$ before retarding to about 0.2 m s^{-1} 10 days later. In contrast, the modeled currents accelerate to about 0.6 m s^{-1} and only decrease to about 0.4 m s^{-1}. This difference may be due to the inadequate representation of the alongshore pressure gradient in the model, as discussed in section 3 and appendix D. Alternatively, an inadequate representation of spatially local and temporally intermittent frictional processes over small-scale topographic features such as Stonewall Bank (124.4°W, 44.5°N) (Moum and Nash 2000; Nash and Moum 2001) that cannot adequately be resolved on a 2 km grid may explain why the v is not sufficiently arrested after the 12 July upwelling. Nash and Moum (2001) demonstrate

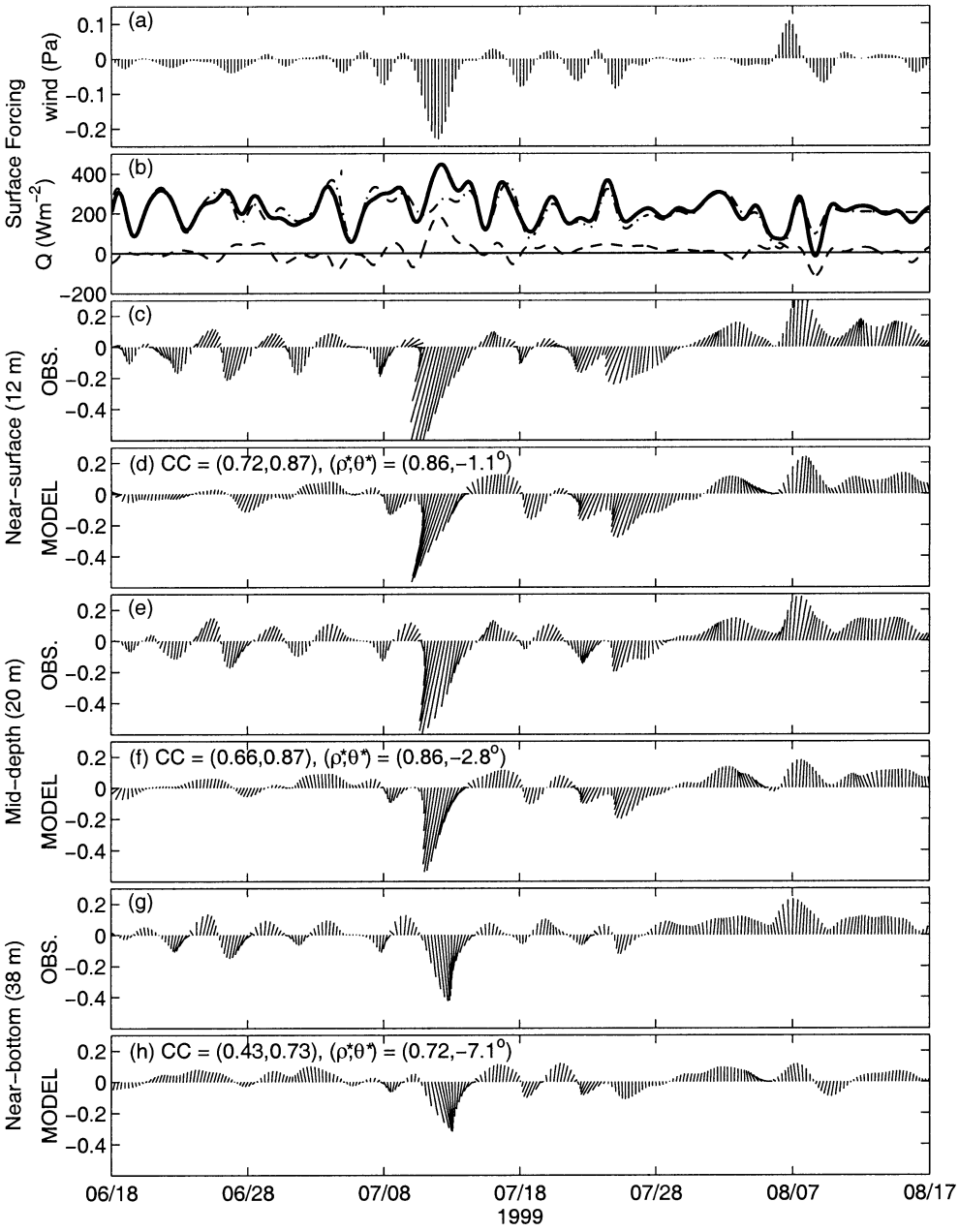

FIG. 6. Time series for expt 6 at the IS mooring of (a) τ^{Sy}, (b) Q (solid), $Q_{lwnet} + Q_{sen} + Q_{lat}$ (dashed), and Q_{sw} (dashed–dotted); observed and modeled currents at (c), (d) 12-m, (e), (f) 20-m, and (g), (h) 38-m depth. CC (.,.) denotes the cross-correlation between the observed and modeled (u, v) and (ρ^*, θ^*) denote the amplitude and phase of the complex cross-correlation.

that the magnitude of bottom stress in the vicinity of Stonewall Bank varies significantly in time and that sometimes the bottom stress is 20 times higher than the background level. Limited measurements of these highly time-dependent small-scale processes makes parameterization of their effects on bottom stress a difficult task.

6) TEMPERATURE AT THE IS AND MS MOORINGS

Time series of observed and modeled (expt 6) θ at the IS and MS moorings are presented in Fig. 8 showing the applied surface forcing, near-surface (2 m), mid-depth (16 m) and near-bottom (40 and 70 m) observed and modeled θ. Near the surface there is good quantitative agreement between the modeled and observed θ (hereafter θ^S) at both the IS and MS mooring, with correlations of 0.93 and 0.76, respectively. The modeled θ^S is typically too warm, particularly after 28 July. In this period the observed meteorological variables were not measured due to instrument failure and so the mean values were used to formulate the heat flux at this time. The correlation between the observed and modeled θ at

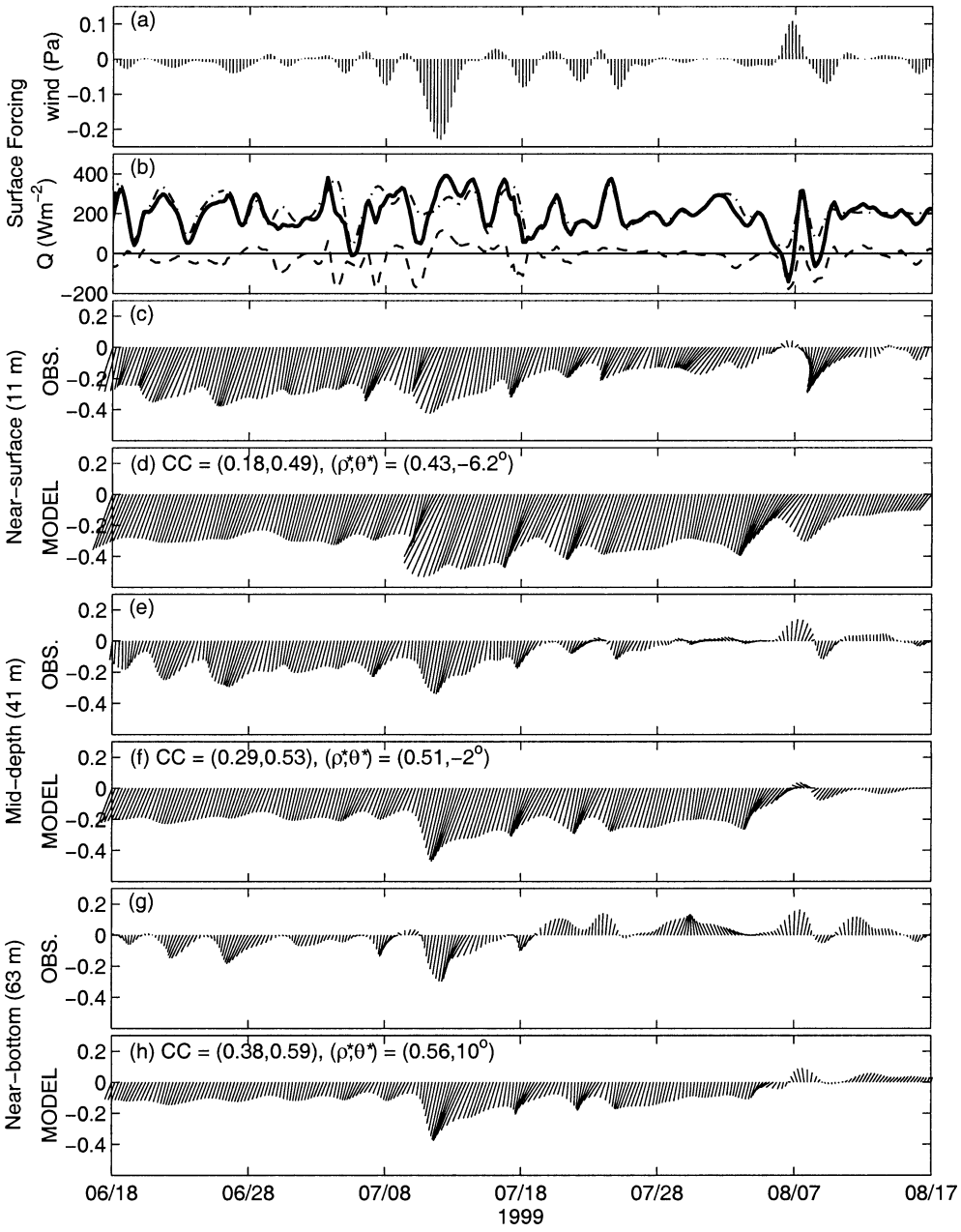

FIG. 7. As for Fig. 6 showing the observed and modeled (expt 6) currents at the MS mooring at (c), (d) 11-m, (e), (f) 41-m, and (g), (h) 63-m depth.

middepth and near the bottom are 0.62 and 0.72, respectively, on the IS mooring. During the 12 July upwelling θ^S decreases by greater than 4° and 5°C at the IS and MS mooring. During the relaxation from upwelling θ^S increases by greater than 5° and 6°C att he IS and MS moorings, respectively. During this relaxation, the contributions from Q_{lwnet}, Q_{sen}, and Q_{lat} are positive indicating that the observed air temperature is warmer than the modeled θ^S, and is acting to heat the ocean surface through a nonradiative heat flux. After 28 July, when τ^{Sy} is near zero, θ^S gradually increases by about 6°C over a three-week period. The most notable change in θ at middepth at the IS mooring is a gradual increase of about 2°C between the 12 July upwelling and the end of the time series. Initially, this increase appears to be adequately represented by the model. It indicates that either the effects of surface heating are penetrating to 16-m depth or warm water is being advected into the region. In the model, θ increases relatively quickly at middepth following the 7 August downwelling event, indicating that warm surface water is either being vertically mixed over the innershelf, or warm water from off-shore is being advected on-shore and downwelled. In the observations the gradual in-

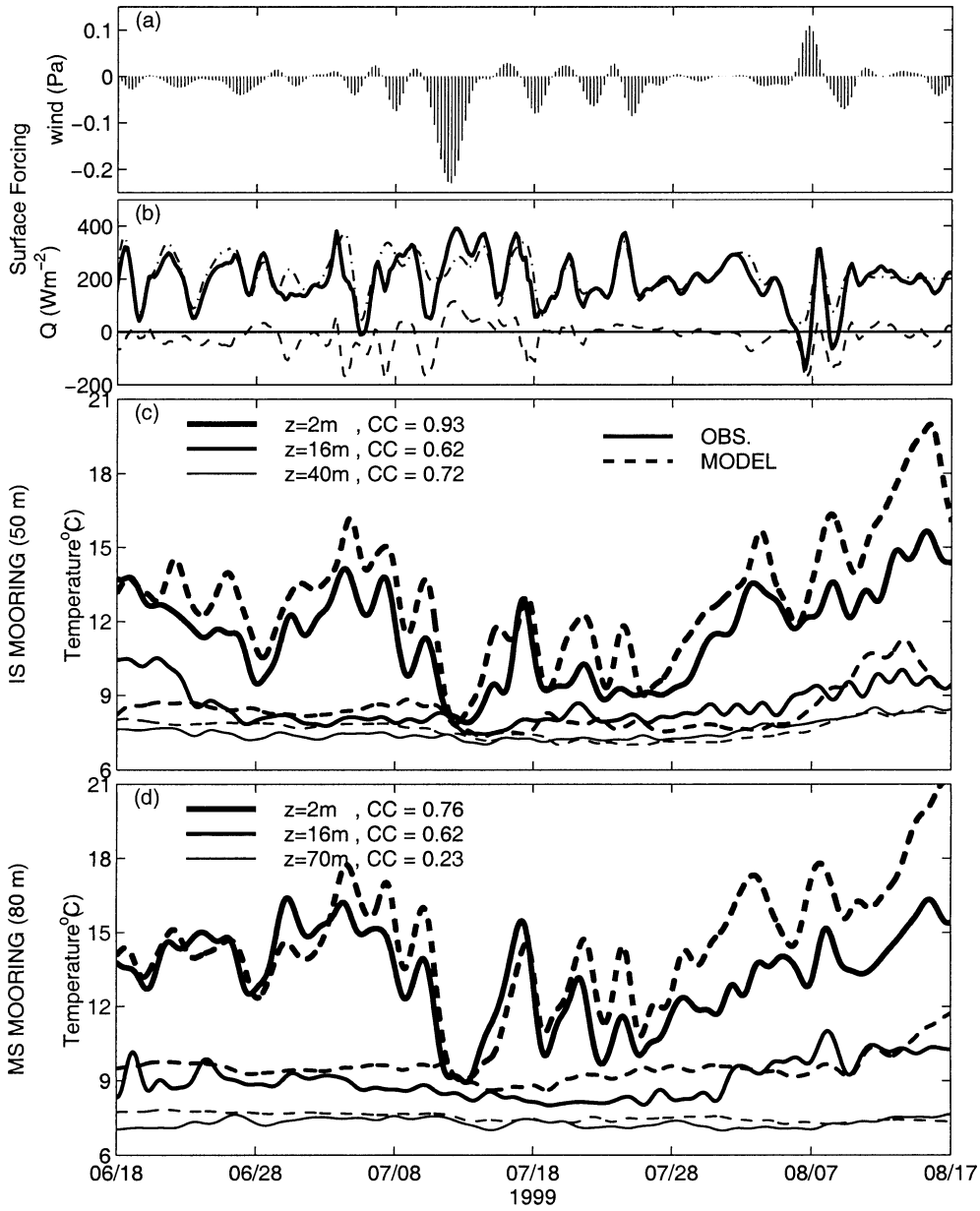

FIG. 8. Time series for expt 6 of (a) τ^{Sy}, (b) Q (solid), $Q_{lwnet} + Q_{sen} + Q_{lat}$ (dashed), and Q_{sw} (dashed-dotted); observed and modeled temperatures at (c) 2-m, 16-m, and 40-m depth on the IS mooring and (d) 2-m, 16-m, and 70-m depth on the MS mooring. The cross-correlation for each model–data pair is shown.

crease in θ starts before the downwelling and during the period of northward flow over the innershelf indicating that warm water is probably being advected into the region. This subtle difference suggests that the model and observations may be representing this warming event through somewhat different mechanisms.

At the MS mooring at middepth and near the bottom the correlation is 0.62 and 0.23, respectively, indicating that the observed variability is well represented by the model at middepth but poorly represented near the bottom. However, the variance of θ at middepth and near the bottom is small compared to θ^S on both moorings.

c. Statistical comparisons with mooring time series

The mean and standard deviations of modeled (expt 6) and observed u, v, and θ and the cross-correlations between modeled and observed variables from the IS and MS mooring locations are plotted as a function of depth in Figs. 9 and 10, respectively. The mean and standard deviations of θ are in good agreement with the observations at both moorings. These fields indicate that most of the variability in the modeled θ occurs in the top 20 m of the water column, presumably due to effects of surface heating and wind mixing. The correlation between modeled and observed θ at the IS mooring is

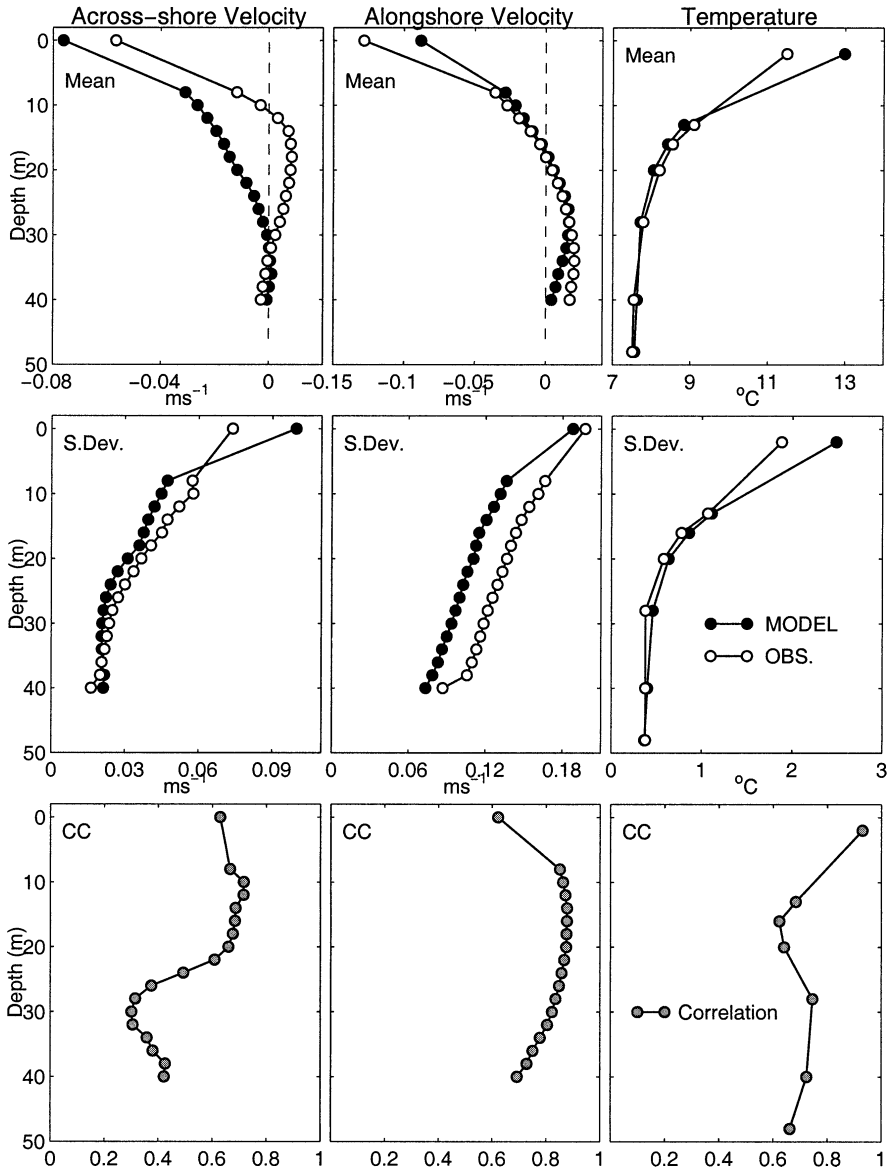

FIG. 9. Modeled (black) and observed (white) mean (top), standard deviation (middle), and CC (bottom, gray) between modeled and observed u (left), v (middle), and θ (right) from the IS mooring. Comparisons at zero depth utilize u and v derived from the CODAR system. The zero line is denoted by a vertical dashed line where appropriate.

greater than 0.6 at all depths. Similarly, the correlation between modeled and observed θ at the MS mooring is greater than 0.6 over the top 20 m of the water column, but is low below that.

The mean and standard deviations of v are in good agreement with the observations at the IS mooring, although the standard deviations of the modeled v are typically 0.025 m s^{-1} less than the observed v. The cross-correlations between the modeled and observed v at the IS mooring are greater than 0.6 at all depths and are greater than 0.8 at middepths. At the IS mooring the mean modeled u shows an offshore flow above 30-m depth and an onshore flow below that, while the observed mean u shows onshore flow below 10-m depth. The structure of the mean u is qualitatively similar to mean fields observed during CUE-II over the midshelf (Smith 1974). In both cases the depth average of u is not zero indicating that the mean across-shore circulation is not two-dimensional in the x–z plane. The observed and modeled standard deviations of u at the IS mooring are in good agreement. The cross-correlation between the modeled and observed u at the IS mooring are greater than 0.6 over the top half of the water column with a lower correlation near the bottom.

The comparison between the modeled and observed mean v at the MS mooring (Fig. 10) shows that the model overestimates the strength of the southward coastal jet by 0.09 m s^{-1}. The mean modeled and ob-

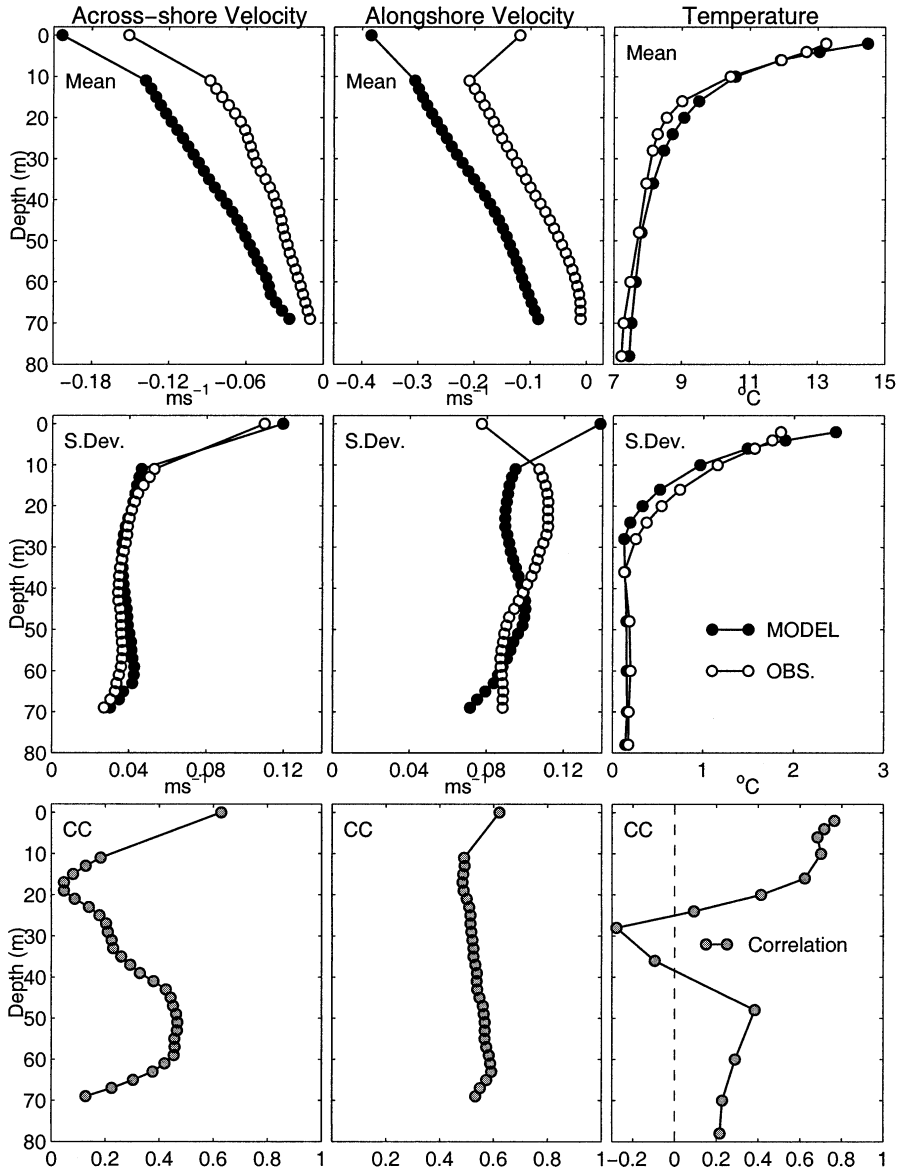

FIG. 10. As for Fig. 9 except for the MS mooring.

served $\partial v/\partial z$ agree well, indicating that the mean modeled and observed $\partial \rho/\partial x$ are also likely to compare favorably by Eq. (5.6). The fact that the bias between the modeled and observed v at the MS mooring is independent of depth suggests that the source of this bias is the inadequate representation of a force affecting the depth-averaged currents, such as the alongshore pressure gradient or bottom stress. The comparison of the mean modeled v near the bottom of the MS mooring demonstrates that the mean bottom stress in the model is greater than in the real ocean. This would excessively retard the modeled v. Therefore, assuming that the parameters in the bottom stress formulation are appropriate, we conclude that the barotropic bias in v is due to a poorly represented alongshore pressure gradient. Net alongshore pressure gradients cannot be correctly represented in a model with periodic alongshore boundary conditions as noted in section 3. The modeled and observed mean u are both directed offshore at all depths. The model overestimates the strength of the offshore flow by 0.02–0.05 m s^{-1}. The standard deviations of the modeled and observed u and v at the MS mooring are generally in good agreement.

d. Comparisons with hydrographic surveys

The mean and first EOF mode of θ for the MiniBAT surveys are presented in Fig. 11 showing the observed and modeled (expt 6) fields and the time series of τ^{Sy} and the modal amplitudes. The mean θ is well represented by the model across the shelf and the modeled and observed mode-1 EOFs show good quantitative agreement.

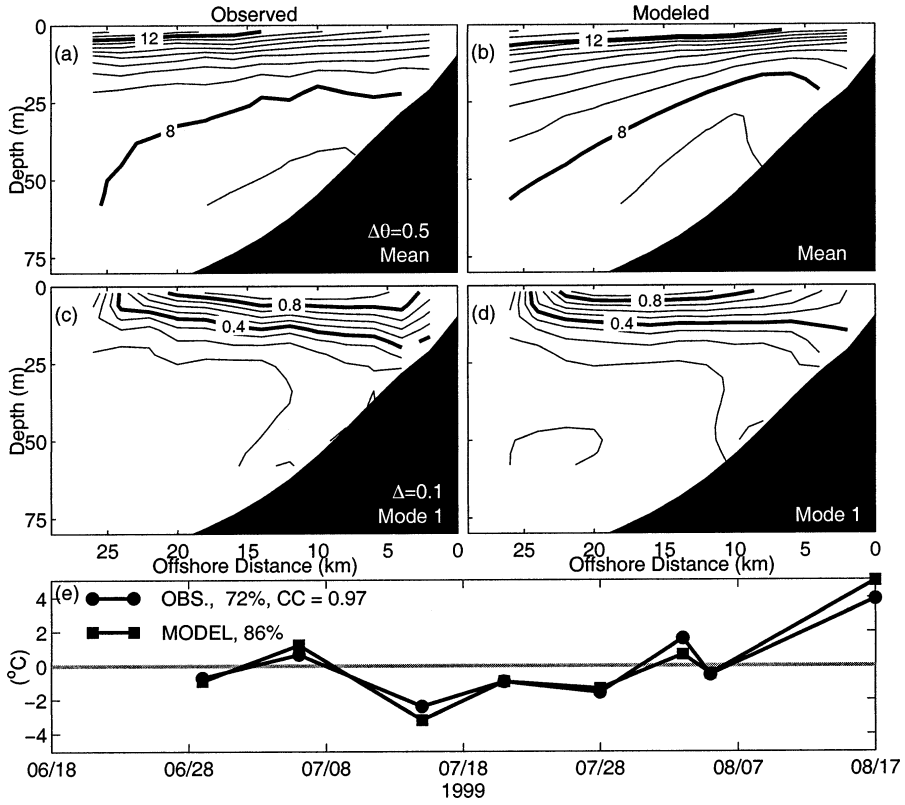

FIG. 11. Observed (left) and modeled (right) (a), (b) mean and (c), (d) mode-1 EOF of θ from the MiniBAT surveys; (e) mode-1 amplitudes for expt 6 showing the percentage of total variance explained by each mode and the correlation between the modal amplitudes.

The first EOF represents 86% and 72% of the total modeled and observed variance, respectively. These modes demonstrate that the dominant fluctuations in θ occur near the surface. The modal amplitudes are in good quantitative agreement with a correlation of 0.97. During the dominant upwelling favorable winds, the amplitude of mode 1 is negative, representing a near-surface θ decrease from the mean by 2°C. This decrease probably represents the combined effects of surface heating, deepening of the wind-driven surface mixed layer, across-shore displacement of the upwelling front, and upwelling. All of these physical processes are expected to be well correlated. Correlation between surface heating and wind-driven upwelling off northern California was noted by Beardsley et al. (1998). The cross-correlation between τ^{Sy} and Q_{tot} for this study varies considerably with space due the dependence on the modeled surface temperature and is -0.46 and -0.3 at the IS and MS moorings, respectively.

An additional comparison between the observed and modeled σ_θ from the MiniBAT surveys on 6 and 15 July, before and after the 12 July upwelling, is presented in Fig. 12. These fields show good qualitative agreement in terms of the spatial details of the sections. Both sections demonstrate the significant variations in the subsurface σ_θ. In light of the comparisons of θ above, it is clear that subsurface σ_θ fluctuations are controlled by the wind-forced circulation through salinity. Both the modeled and observed σ_θ fields show an isolated mass of dense water, with $\sigma_\theta > 26.5$ kg m^{-3}, over the midshelf. This feature was also observed during CUE-I (Huyer 1973). In Part II of this study (Oke et al. 2002a), we demonstrate that this dense water is upwelled to the north of Newport and is advected southward beneath the coastal jet.

An example of a comparison between the observed and modeled surface σ_θ for the 23–26 July SeaSoar survey is shown in Fig. 13. For these comparisons, the observed survey took about 2.3 days to complete for the survey track shown in Fig. 2. The model fields presented here are constructed using the same sampling strategy as the SeaSoar survey. While the details of these modeled and observed fields differ, the fields are qualitatively similar. For example, both show denser water penetrating over Heceta Bank at about 44.2°N, and both have contours that reflect the alongshore variations in topography and both show a hint of an eddy over Heceta Bank.

e. Comparison with CODAR data

Comparisons between HF-radar derived surface currents from the CODAR array and modeled surface currents are shown in Figs. 14 and 15. Figure 14 shows the magnitude and phase of the complex cross-correlation

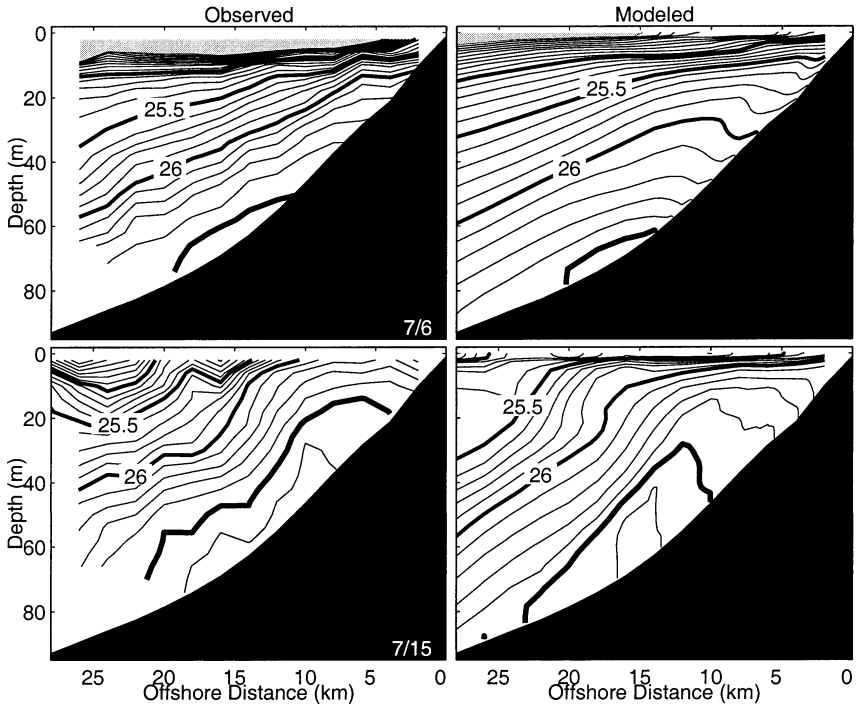

FIG. 12. Observed (left) and modeled (right) σ_θ off Newport during the 6 and 15 Jul MiniBAT surveys, before and after the 12 Jul upwelling ($\Delta\sigma_\theta$ = 0.1 kg m^{-3}; the 25, 25.5, 26, and 26.5 σ_θ contours are bold). Regions where $\sigma_\theta < 24$ kg m^{-3} are shaded in gray.

between the observed and modeled surface currents. The correlation between the modeled and observed currents is greater than 0.5 over most of the CODAR region. The highest correlation is in excess of 0.7 over the innershelf. The lowest correlation is at the southern end of the CODAR region, where the correlations are less than 0.5. The phase angles between the observed and modeled currents are typically less than 10°.

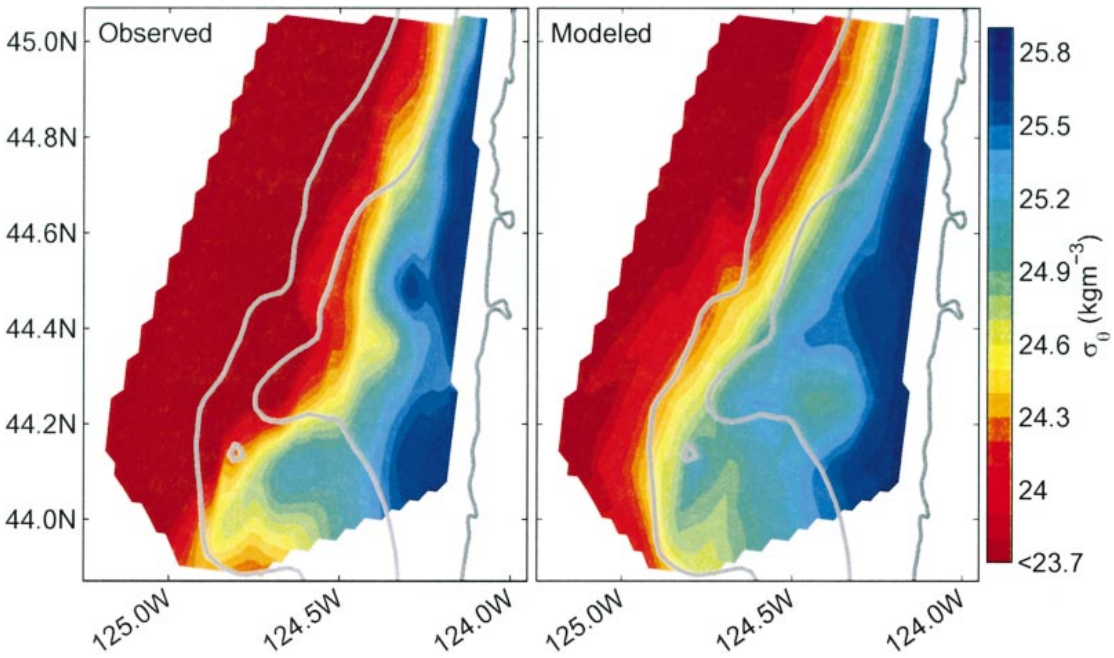

FIG. 13. Observed (left) and modeled (right) surface σ_θ (1-m depth) for the period between 23 and 26 Jul. The SeaSoar survey track is shown in Fig. 2. The model field is constructed using the same sampling strategy as the SeaSoar survey. The 100-m and 200-m isobaths are gray.

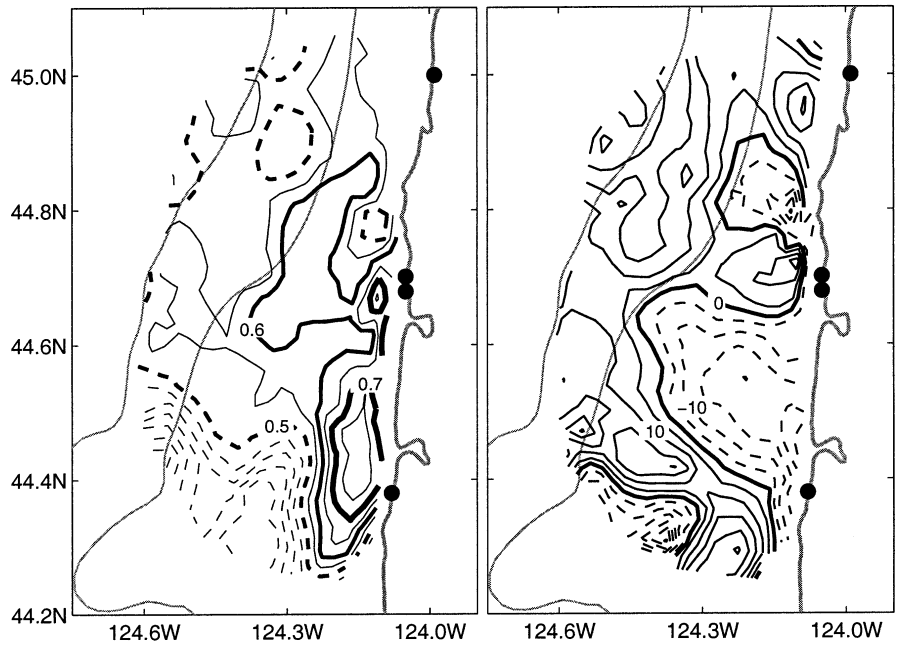

FIG. 14. The magnitude (left) and phase (right) of the complex cross-correlation between the modeled and observed surface currents. For the amplitude, the contour intervals are 0.05 and the thin dashed contours are <0.5; for the phase the contour intervals are 5°, the zero contour is bold, and the dashed contours are negative. The mean magnitude is 0.53 and the rms phase is 4.5°. The approximate land-based radar locations are shown (•).

An EOF analysis of the observed and modeled surface currents in the CODAR region is presented in Figure 15 showing the mean fields, the first two dominant EOF modes and the corresponding modal amplitudes. The divergence of the observed and modeled means and EOFs are also contoured. The rms amplitude of the EOF modes are used to scale the normalized EOFs for this calculation. The mean observed currents are typically weaker than the mean modeled currents. However, there is some indication from the fields presented in Fig. 10 that the mean (u, v) from the CODAR may underestimate the true mean field. This may be a result of processing difficulties that were encountered during the summer 1999 field season. As expected, the surface currents are ageostrophic in both the modeled and observed fields, as indicated by the nonzero divergence. Both the modeled and observed mean divergence fields show positive divergence (upwelling), with comparable magnitudes, over the innershelf and a weak convergence offshore. The observations show that the mean upwelling occurs on the shelf over a fairly broad area with a local maximum to the north of Newport. The modeled field also has a local maximum located to the north of Newport, but has the upwelling occurring along the shoreward edge of the coastal jet. Clearly the observed mean divergence varies in the y direction, indicating that the across-shore circulation is not two-dimensional in the x–z plane. Interestingly, the observed mean divergence is most variable in the y direction to the north, where the isobaths are most uniform in the y direction. It is not clear whether this variability is real, or an artifact of the observing system. Results presented in Part II of this study, however, demonstrate that the strongest modeled upwelling occurs to the north of Newport suggesting that this feature may be real.

The structure of the observed and modeled mode-1 EOFs are very similar and both have local maxima in the rms divergence to the north of Newport. The modal amplitudes are highly correlated, with a correlation of 0.74. The amplitude of the observed mode-1 variations are typically half the amplitude of the modeled mode-1 variations. When the observed amplitude is regressed onto the modeled amplitude the regression coefficient is 0.47 ± 0.02. The zero-lag correlations between τ^{Sy} and the observed and modeled mode-1 amplitudes is -0.65 and -0.81, respectively. In contrast, the correlations between τ^{Sy} and the observed and modeled mode-2 amplitudes are 0.04 and 0.1, respectively. Clearly, the mode-1 EOFs represent the dominant wind-driven modes.

The structures of the mode-2 EOFs have similar characteristics, such as the convergence/divergence over the inner-shelf. The correlation between the modeled and observed modal amplitudes for mode 2 is 0.53. These modes represent a divergence (positive amplitude) to the north of Newport during the 12 July upwelling. When the mode-2 amplitude is negative there is a convergence to the north of Newport and on the shoreward edge of the coastal jet for the modeled mode-2 EOF. This is reminiscent of the frontal convergence measured using surface drogues around 44.5°N during a 1972 CUE-I study (Stevenson et al. 1974). The qualitative consistency between the modeled and observed con-

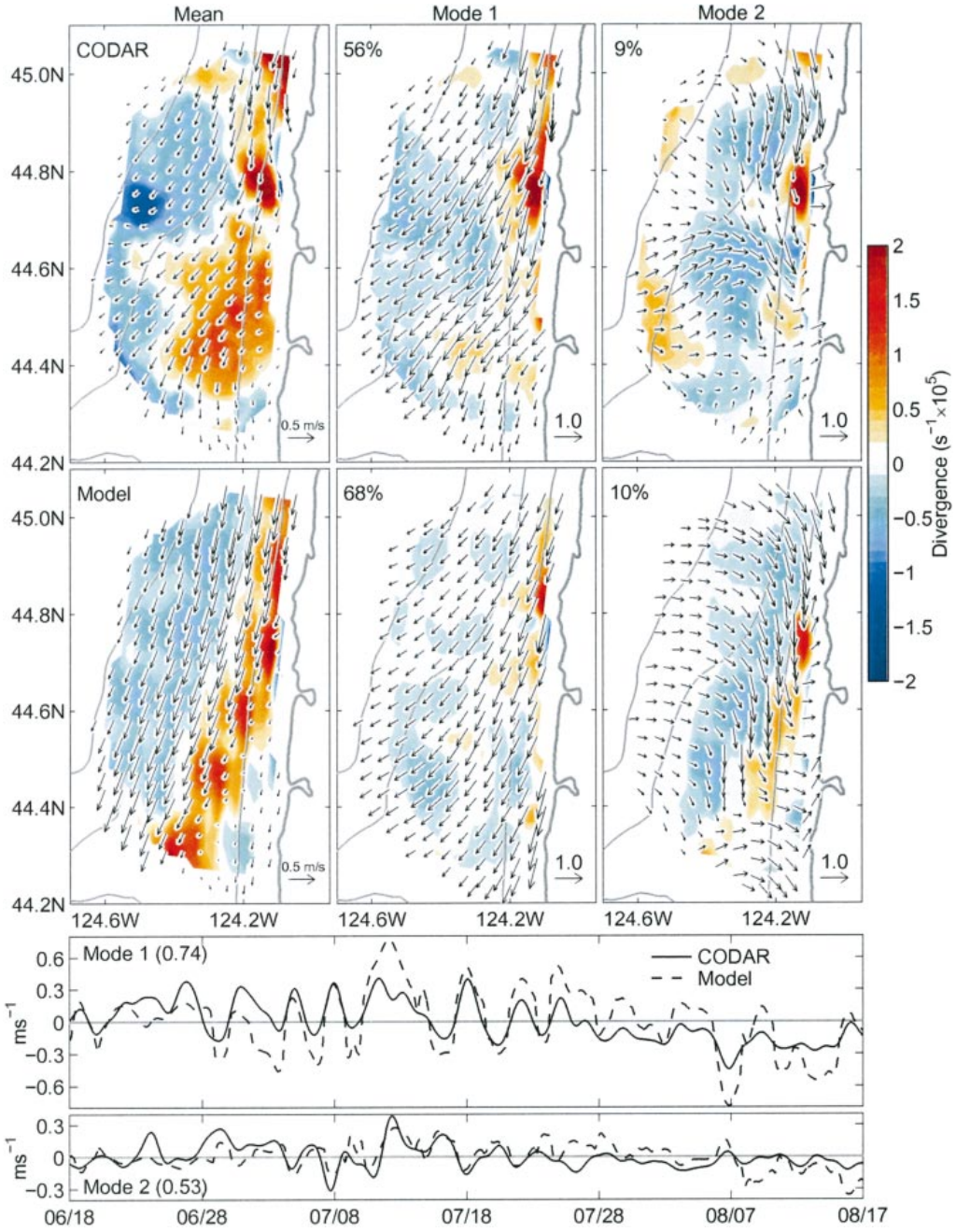

FIG. 15. The mean (left) and dominant normalized EOFs (middle and right) of surface currents from the CODAR observations (top) and the model (expt 6) (middle) as labeled. The divergence calculated from the mean fields and from the EOFs scaled with the rms modal amplitudes are contoured. The percentage of total variance explained by each EOF mode is displayed in each panel. The modal amplitudes of the observed (solid) and modeled (dashed) EOFs are also shown (bottom) and the correlation between the observed and modeled amplitudes are given in parentheses in the bottom panels.

vergence/divergence promotes confidence that both the model and the CODAR system are capable of representing and measuring this important physical process.

f. Frequency domain analysis

Comparisons in the frequency domain, between the demeaned modeled and observed V and θ^S for expt 6, are shown in Fig. 16. The squared coherence $[(\text{coh})^2 = |P_{XY}|^2/(P_{XX}P_{YY})$, where P_{XX} is the smoothed spectral density of a time series X, and P_{XY} is the complex smoothed cross-spectral density between time series X and $Y]$; the phase $\{\text{phase} = \tan^{-1}[-\text{imag}(P_{XY})/\text{real}(P_{XY})]\}$ and the gain $\{\text{gain} = [(\text{coh})^2 P_{YY}/P_{XX}]^{0.5} = [|P_{XY}|/P_{XX}]^2\}$ are calculated in order to assess the model's performance for each resolvable frequency f_q.

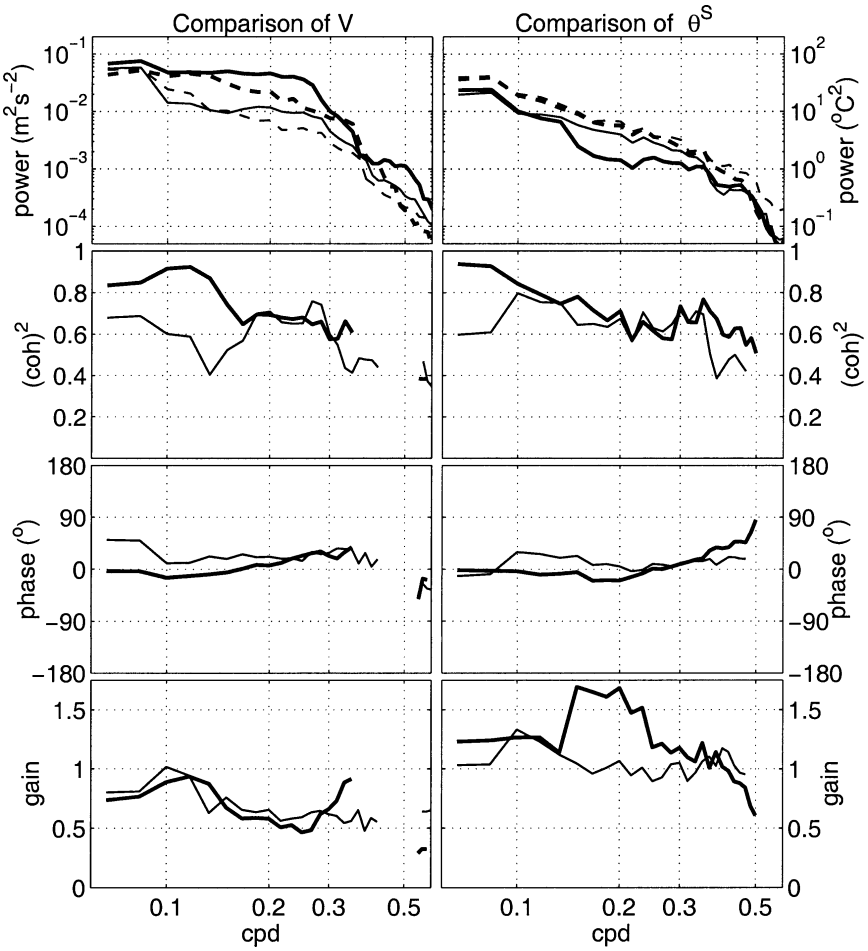

FIG. 16. Frequency domain comparisons of demeaned V (left) and θ^S (right) at the IS (bold) and MS (thin) mooring showing the power spectra, squared coherence $(\text{coh})^2$, phase, and gain (top to bottom). The spectra (top) is shown for both the observed (solid) and the modeled (dashed) fields; the $(\text{coh})^2$, phase and gain are only plotted for frequencies where $(\text{coh})^2$ is above the 95% significance level.

The frequencies of interest for this study are in the band $f_q < 0.6$ cycles per day (cpd). For those frequencies the modeled and observed signals are coherent with near-zero phase. For V the average gain is about 0.65 indicating that the amplitude of the modeled signal is about 65% of the amplitude of the observed signal. For θ^S however the average gain is 1.18 at the IS mooring and 1.06 at the MS mooring indicating the amplitude of the modeled θ^S fluctuations are generally greater than the amplitude of the observed θ^S for the frequencies of interest.

6. Summary

The modeled fields show good quantitative agreement with observed fields from the IS mooring, with correlations for u, v, and θ as high as 0.72, 0.87, and 0.93, respectively. Good quantitative agreement between modeled and observed fields are also found for the MiniBAT hydrographic surveys. Good qualitative agreement is found between observed and modeled fields from the MS mooring, the SeaSoar hydrographic surveys, and the CODAR measurements. Additionally, we show that the modeled V and θ^S fields are consistent with observations at both the IS and MS moorings for all of the resolvable frequencies of interest.

The sensitivity study shows that surface heating is important and that the model results are sensitive to initial stratification. This dependence on initial stratification has implications for data assimilation studies (e.g., Oke et al. 2002b), suggesting that corrections to initial stratification using an objective strong constraint assimilation approach for coastal systems has considerable potential value. Moreover, we find that utilizing τ^{Sy} with an idealized across-shore structure improves the modeled θ fields over the midshelf, and that utilizing idealized river forcing improves the mean σ_θ field off Newport. The comparisons for the experiment with river forcing demonstrates that in the vicinity of Newport the Columbia River plume is typically located greater than

15 km from the coast and is isolated to the top few meters of the water column.

The MiniBAT comparisons demonstrate that the dominant θ fluctuations occur near the surface, while subsurface fluctuations in σ_θ are controlled by salinity. Additionally, the MiniBAT comparisons show that sub-26.5 σ_θ water, near the bottom over the mid-to innershelf is isolated from water of the same density directly offshore of Newport. This suggests that this water is not uplifted off Newport, but arrives at the Newport hydrographic line through alongshore advection. This demonstrates that the dominant upwelling circulation off Newport is not two-dimensional in the x–z plane as standard conceptual models assume, but is highly three-dimensional. This aspect of the modeled circulation is investigated in detail in Part II of this study.

The comparisons with surface currents derived from the CODAR system demonstrate that the magnitude of divergence, an indicator for the strength of upwelling, varies in the y direction with a maximum in the mean and fluctuating components to the north of Newport. This result suggests that upwelling is stronger to the north where the continental shelf is narrower and more uniform in the y direction. This aspect of the circulation is consistent with the implied three-dimensionality of the upwelling referred to above and is investigated in detail in Part II of this study.

Acknowledgments. This research was supported primarily by the National Oceanographic Partnership Program (NOPP) through ONR Grant N00014-98-1-0787. Support was also provided by the ONR Ocean Modeling and Prediction Program through Grant N00014-98-1-0043 and by an ONR DURIP Grant N00014-99-1-0773. The authors gratefully acknowledge Roger Samelson for providing modeled wind fields for the sensitivity study.

APPENDIX A

Heat Flux Formulation

The net surface heat flux Q is the sum of the incoming shortwave radiation Q_{sw}, the net longwave radiation Q_{lwnet}, the sensible heat flux Q_{sen}, and the latent heat flux Q_{lat}:

$$Q = Q_{\text{sw}} + Q_{\text{lwnet}} + Q_{\text{sen}} + Q_{\text{lat}}.$$

The net surface heat flux can be thought of as a balance between the heating from the sun and the heating due to the equilibration between the atmosphere and the ocean temperatures. The equilibration acts to reduce the difference between the near-surface air temperature T_a and the ocean surface temperature T_s. These components of Q are given by

$$\begin{aligned}
Q_{\text{sw}} &= Q^o_{\text{sw}} \\
Q_{\text{sen}} &= \rho_a c_{ap} C_h (T^o_a - T^m_s)|\mathbf{v}^o_a - \mathbf{v}^m_s| \\
Q_{\text{lat}} &= Q_{\text{sen}}/R \\
Q_{\text{lwnet}} &= [\epsilon\sigma(T^o_a)^4(0.39 - 0.05e^{0.5}) \\
&\quad + 4\epsilon\sigma(T^o_a)^3(T^m_s - T^o_a)](1 - b\overline{C}) \\
\overline{C} &= [1 - (\overline{I}^o_{\text{sw}}/\overline{I}_{\text{swcs}}) + 0.0019\alpha]/0.62,
\end{aligned}$$

where superscripts m and o denote modeled and observed respectively; ρ_a is the density of air (1.3 kg m^{-3} Gill 1982); c_{ap} is the heat capacity of air (1010 J K^{-1} kg^{-1}); c_{wp} is the heat capacity of water (4160 J K^{-1} kg^{-1}); C_h is the sensible heat flux transfer coefficient ([0.83–1.1] $\times$ 10^{-3} Gill 1982); here 1 $\times$ 10^{-3}); $|\mathbf{v}^o_a - \mathbf{v}^m_s|$ is the magnitude of the wind velocity minus the surface current velocity; R is the Bowen ratio (0.1–0.45 Pickard and Emery 1990; here 0.2); ϵ is emissivity of the ocean surface (0.98; Dickey et al. 1994); σ is the Stefan–Boltzman constant (5.7 $\times$ 10^{-8}; Gill 1982); e is the average vapor pressure (12 mbars, given an average air temperature of 12°C and an average relative humidity of 85%); T^o_a and T^m_s are in kelvins; b is the constant cloud correction factor (0.75; Beardsley et al. 1998); $\overline{C}$ is the daily averaged cloud cover; $\overline{I}^o_{\text{sw}}$ is the observed daily averaged incoming shortwave radiation; $\overline{I}_{\text{swcs}}$ is the daily averaged clear-sky incoming shortwave radiation; α is the local noon solar altitude (radians).

The shortwave extinction coefficient E_{sw} and the shortwave surface transmission coefficient Tr_{sw} are used in the application of penetrating shortwave radiation in POM. For coastal applications with water type III (Jerlov 1976; Simonot and Le Treut 1986) the default E_{sw} and Tr_{sw} are 0.127 and 0.24, respectively, which indicates that the attenuation of Q_{sw} has an e-folding scale of approximately 8 m. The seasonally averaged attenuation of Q_{sw} observed near the surface along the Newport hydrographic line during the summer of 1999 has an e-folding scale of 1.5–2.5 m (Austin et al. 2000), which corresponds to $E_{\text{sw}} = 0.67 - 0.4$ m^{-1}. When implemented into the POM, all heat flux terms are divided by $\rho_w c_{wp} \approx 4.16 \times 10^6$ before being applied.

APPENDIX B

River Input

Forcing for the Columbia River is imposed approximately 35 km from the southern end of the standard model domain (appropriate for periodic boundary conditions). A steady inflow is imposed at a single horizontal grid cell over the entire 10-m depth water column. The imposed flow corresponds to a constant transport of $T = 5819$ m^3 s^{-1} and linearly increases from zero at the bottom to a maximum at the surface:

$$u_{\rm riv} = \frac{-2(\sigma + 1)T}{h\Delta y}, \qquad U_{\rm riv} = \int_{-1}^{0} u_{\rm riv}\, d\sigma,$$

$$\eta_{\rm riv} = \eta_{\rm riv-1}, \qquad \theta_{\rm riv} = \theta_{\rm init}(z), \qquad \text{(B1)}$$

and $v_{\rm riv} = V_{\rm riv} = S_{\rm riv} = w_{\rm riv} = (1/2)q^2_{\rm riv} = q^2 l_{\rm riv} = 0$, where the subscripts ''riv'' denotes the coastal grid points at which the river forcing is applied, the subscript ''init'' denotes the initial value, w is vertical velocity, q^2 is twice the turbulent kinetic energy, and l is the mixing length scale. The depth-averaged inflow velocity $U_{\rm riv} \approx 0.12$ m s^{-1} ($\Delta y = 5$ km, $h = 10$ m).

APPENDIX C

Mean Squared Error

We define the ith modeled and observed variable as m_i and o_i, respectively; $\overline{m}$ and $\overline{o}$ are the respective means; S_m and S_o are the respective standard deviations; and CC is the cross-correlation coefficient between the modeled and observed fields:

$$\text{CC} = S_m^{-1} S_o^{-1} \frac{1}{n} \sum_i^n (m_i - \overline{m})(o_i - \overline{o}), \qquad \text{(C1)}$$

where n is the total number of observations in time and space that can be directly compared with the modeled fields. The MSE can be written in terms of $\overline{m}$, $\overline{o}$, S_m, S_o, and CC (e.g., Murphy 1995):

$$\begin{aligned}
\text{MSE} &= \frac{1}{n}\sum_{i=1}^{n}(m_i - o_i)^2 = \frac{1}{n}\sum_{i=1}^{n} m_i^2 - 2m_i o_{ii} + o^2 \\
&= \frac{1}{n}\sum_{i=1}^{n} m_i^2 - 2\frac{1}{n}\sum_{i=1}^{n} m_i o_i + \frac{1}{n}\sum_{i=1}^{n} o_i^2 \\
&\qquad \left[\text{and } \frac{1}{n}\sum_{i=1}^{n} m_i^2 = S_m^2 + \overline{m}^2\right] \\
&= S_m^2 + \overline{m}^2 - 2\frac{1}{n}\sum_{i=1}^{n} m_i o_i + S_o^2 + \overline{o}^2 \\
&= (\overline{m} - \overline{o})^2 + 2\overline{m}\,\overline{o} + S_m^2 + S_o^2 - 2\frac{1}{n}\sum_{i=1}^{n} m_i o_i \\
&= (\overline{m} - \overline{o})^2 + S_m^2 + S_o^2 \\
&\qquad - 2\left(\frac{1}{n}\sum_{i=1}^{n} m_i o_i - 2\overline{m}\,\overline{o} + \overline{m}\overline{o}\right) \\
&= (\overline{m} - \overline{o})^2 + S_m^2 + S_o^2 \\
&\qquad - 2\left(\frac{1}{n}\sum_{i=1}^{n} m_i o_i - \overline{o}\frac{1}{n}\sum_{i=1}^{n} m_i - \overline{m}\frac{1}{n}\sum_{i=1}^{n} o_i + \overline{m}\,\overline{o}\right) \\
&= (\overline{m} - \overline{o})^2 + S_m^2 + S_o^2 - 2\frac{1}{n}\sum_{i=1}^{n}(m_i - \overline{m})(o_i - \overline{o}) \\
&= (\overline{m} - \overline{o})^2 + S_m^2 + S_o^2 - 2S_m S_o \text{CC} \\
&= (\overline{m} - \overline{o})^2 + (S_m - S_o)^2 + 2S_m S_o(1 - \text{CC}) \\
&= \text{MB}^2 + \text{SDE}^2 + 2S_m S_o(1 - \text{CC}),
\end{aligned}$$

where $\text{MB} = (\overline{m} - \overline{o})$ and $\text{SDE} = (S_m - S_o)$ are the model bias and standard deviation error respectively.

APPENDIX D

Sensitivity Study

a. Sensitivity to the extinction coefficient

The experiment pairs 2–3, 5–6, 8–9, and 11–12 have identical initial stratification and wind forcing with a different extinction coefficient for $Q_{\rm sw}$. Heat from $Q_{\rm sw}$ is distributed with an e-folding scale of 8 and 1.5 m for $Q_{\rm III}$ and $Q_{\rm Obs}$, respectively. Applying $Q_{\rm Obs}$ should result in a shallower, more stably stratified surface mixed layer compared to $Q_{\rm III}$. This difference is expected to change the modeled variables near the surface, potentially reducing the amount of momentum that penetrates over depth. The potential effects of varying the extinction coefficient on the response of the surface mixed layer is demonstrated by Martin (1985). Near-surface model–data comparisons at the moorings are limited to near-surface temperature θ^S (at 2-m depth). The shallowest reliable observations of u and v at the moorings are at approximately 10-m depth (Fig. 3). We find that varying the extinction coefficient has only a slight effect on the MB (5.2), SDE (5.3) or CC. In general, there is a slight improvement in the model–data comparisons when $Q_{\rm Obs}$ is used in place of $Q_{\rm III}$ (Table 2). In this study the wind stress is clearly the dominant forcing term for the continental shelf circulation. The strong wind stress acts to mix θ in the near-surface layer, effectively redistributing the near-surface heat evenly over the well-mixed surface layer, negating the effects of varying the extinction coefficient. The effects of varying the extinction coefficient may be more important for regions where wind forcing is less dominant.

b. Sensitivity to initial stratification

As noted in the section 5, varying the initial stratification has a significant effect on the model skill (Table 2), with the average SS ranging from approximately -0.4 (expts 2–3), 0.3 (expts 5–6), 0.16 (expts 8–9), and 0.27 (expts 11–12) for experiments with surface heating and different initial stratification. These variations are mainly due to differences in CC and MB/S_o at the IS mooring (Fig. D1).

For the experiments with no surface heating (expts 1, 4, 7, 10, and 18), expt 1, with $(\theta, S)_{73}$ initial stratification, performs the best. Figure 4 shows that near the surface $(\theta, S)_{73}$ is considerably warmer than the other initial profiles, and is several degrees warmer than true ocean state, approximately represented by $(\theta, S)_{99}$. In the absence of surface heating we expect the wind to vertically mix the water column near the surface and to entrain colder water from below into a surface mixed

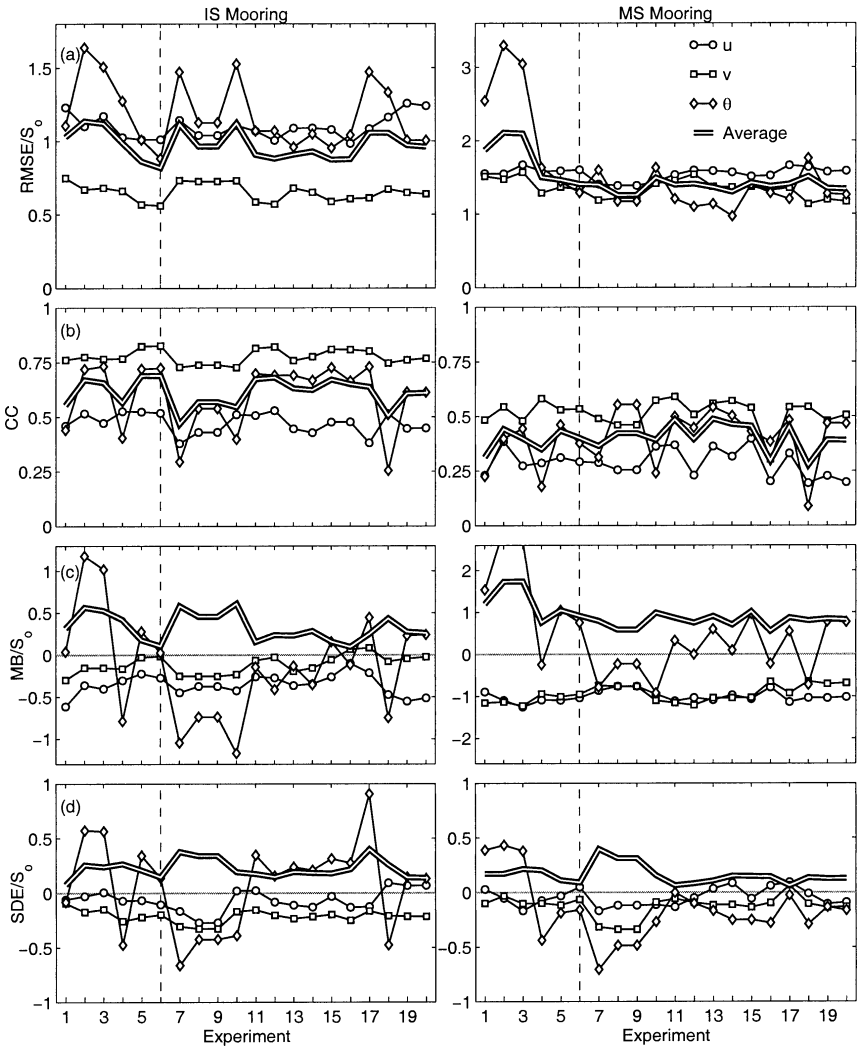

FIG. D1. Depth-averaged statistics for u (circles), v (squares), and θ (diamonds) from the IS (left) and MS (right) moorings for each experiment (see Table 1 for experiment descriptions) showing the (a) normalized RMSE, (b) CC (C1), (c) normalized MB (5.2), and (d) normalized SDE (5.3). The average or rms, where appropriate, of each statistic over all variables is shown. The experiment analyzed in detail in Part II of this study is denoted by the vertical dashed line.

layer acting to decrease the near-surface θ over time. Because $(\theta, S)_{73}$ is too warm, after this mixing and entrainment expt 1 is more consistent with the true ocean than the other experiments with no surface heating. We suggest that using an initial θ profile that is too warm is representing the integrated effects of surface heating.

When $(\theta, S)_{73}$ initial stratification is used and surface heating is applied (expts 2–3) the results are worse than expt 1, with no surface heating. For these experiments the effects of surface heating are effectively included twice; through the initial stratification, as discussed above, and through the application of a surface heat flux. This is supported by the fact that CC is higher for θ in expts 2 and 3 compared to expt 1 (heating does improve the modeled fluctuations) but MB/S_o is greater for θ in expts 2 and 3 compared to expt 1 (heating makes the model too warm).

For experiments with initial stratification that differ from $(\theta, S)_{73}$ (expts 4–6, 7–9, 10–12) the inclusion of surface heating (expts 5–6, 8–9, 11–12) improved the model skill for every case. For θ, in all of these cases CC increased, MB/S_o decreased, and SDE/S_o decreased. From these experiments, it is clear that appropriate initial stratification and surface heating is important for the success of the model. An explanation for why initial stratification is important is provided in section 5.

c. Sensitivity to spatially variable wind forcing

Experiments 13–14 utilize $\tau^{Sy}(x)$, but are otherwise equivalent to expts 5–6. Experiments 13–14 have a lower average SS than expts 5–6 indicating that the inclusion of across-shore structure to τ^{Sy} does not improve the overall agreement between modeled and observed

fields. However, the SS of expts 13–14 for θ from the MiniBAT surveys and from the MS mooring (Table 2) are greater than any other experiment considered in this study indicating that using $\tau^{Sy}(x)$ improves the modeled θ over the midshelf. Experiments 16 and 17 are compared in order to further assess the effects of $\tau^{Sy}(x)$. Both of these experiments also utilize idealized river forcing. For these cases the average SS is again lower when $\tau^{Sy}(x)$ is utilized. However the SS for θ from the MiniBAT surveys and from the MS mooring is again improved. The comparison with the MiniBAT surveys presented in Fig. 5 suggests that there is no notable qualitative benefit to $\tau^{Sy}(x)$ in the mean and standard deviation of σ_θ, however the SS assessment demonstrates a quantitative improvement that is probably due to improvements in CC from Eq. (5.4).

d. Sensitivity to river forcing

In order to reliably represent river forcing an iterative upstream advection scheme (Smolarkiewicz 1984) for θ and S is used in expts 16 and 17 that only differ from expts 6 and 14, respectively, in the inclusion of idealized river forcing. In both cases the inclusion of idealized river forcing degrades the solution, resulting in a lower average SS. However, for this case with $\tau^{Sy}(x)$ (expt 17) the SS for S from the MiniBAT surveys is greater than any other experiment considered in this study. Additionally, the comparisons with the MiniBAT surveys in Fig. 5 indicate that expt 16 has the best qualitative agreement with observations in both the mean and standard deviation of σ_θ. These considerations demonstrate that there is some benefit to the inclusion of river forcing and that further development in this area is likely to be worthwhile.

e. Sensitivity to across-shore wind forcing

Experiments 15 and 20 differ from expts 6 and 19, respectively, only in the inclusion of τ^{Sx}. For both pairs of experiments the addition tended to degrade the results. One reason for this might be that the assumption of spatial uniformity for τ^{Sx} is invalid, while this assumption for τ^{Sy} is tolerable. With the improvement of regional mesoscale atmospheric models (e.g., Samelson et al. 2002) the validity of this assumption can be more fully assessed.

f. Sensitivity to domain size

Experiments 18 and 19 differ from expts 4 and 6 only in that they utilize the EDM described in section 3. Although, the results from the EDM generally compare less favorably with observations than the standard domain model, there are some indications that the larger domain may be beneficial. For example, expts 18 and 19 have more skill than expts 4 and 6 for v at the MS mooring. This is because the MB is smaller for expts 18 and 19 compared to expts 4 and 6 (Fig. D1). This may be due to the improved representation of alongshore pressure gradients that arrest the alongshore flow. The comparisons with the MiniBAT surveys (Fig. 5) suggest that utilizing the EDM does not qualitatively affect the mean and standard deviation of σ_θ off Newport.

REFERENCES

Austin, J. A., J. A. Barth, and S. D. Pierce, 2000: Small-boat hydrographic surveys of the Oregon mid- to inner-shelf. Oregon State University Data Rep. 178, 00-2, 99 pp.

Barth, J. A., R. O'Malley, A. Y. Erofeev, J. Fleischbein, S. D. Pierce, and P. M. Kosro, 2001: SeaSoar CTD observations from the Central Oregon Shelf, W9907C, 13–31 July 1999. Oregon State University Data Rep. 184, 01-5, 355 pp.

Beardsley, R. C., E. P. Dever, S. J. Lentz, and J. P. Dean, 1998: Surface heat flux variability over the northern California shelf. *J. Geophys. Res.*, **103,** 21 553–21 586.

Blumberg, A. F., and G. L. Mellor, 1987: A description of a three-dimensional coastal ocean circulation model. *Three-Dimensional Coastal Ocean Models*, N. Heaps, Ed., Vol. 4, Amer. Geophys. Union, 1–16.

Boyd, T., M. D. Levine, P. M. Kosro, and S. R. Gard, 2000: Mooring observations from the Oregon continental shelf. Oregon State University Data Rep. 177, 00-1, 216 pp.

Chapman, D. C., 1985: Numerical treatment of cross-shelf open boundaries in a barotropic coastal ocean model. *J. Phys. Oceanogr.,* **15,** 1060–1075.

Dickey, T. D., D. V. Manov, D. A. Siegel, and R. A. Weller, 1994: Determination of longwave heat flux at the air–sea interface using measurements from buoy platforms. *J. Atmos. Oceanic Technol.,* **11,** 1057–1078.

Federiuk, J., and J. S. Allen, 1995: Upwelling circulation on the Oregon continental shelf. Part II: Simulations and comparisons with observations. *J. Phys. Oceanogr.,* **25,** 1867–1889.

Gan, J., and J. S. Allen, 2002: A modeling study of shelf circulation off northern California in the region of the Coastal Ocean Dynamics Experiment. Part 1: Response to relaxation of upwelling wind. *J. Geophys. Res.*, in press.

Gill, A. E., 1982: *Atmosphere–Ocean Dynamics.* Academic Press, 662 pp.

Halpern, D., 1976: Measurements of near-surface wind stress over an upwelling region near the Oregon coast. *J. Phys. Oceanogr.,* **6,** 108–112.

Huyer, A., 1973: Vertical distributions of temperature, salinity and sigma-t from observations from R/V Yaquina during coastal upwelling experiment. Oregon State University Data Rep. 6, 73-6, 59 pp.

——, 1983: Coastal upwelling in the California Current System. *Progress in Oceanography,* Vol. 12, Pergamon, 259–284.

Jerlov, N. G., 1976: *Marine Optics.* Elsevier Oceanography Series, Vol. 14, Elsevier, 231 pp.

Kosro, P. M., J. A. Barth, and P. T. Strub, 1997: The coastal jet: Observations of surface currents along the Oregon Continental Shelf from HF radar. *Oceanography,* **10,** 53–56.

Kundu, P. K., 1976: Ekman Veering observed near the ocean bottom. *J. Phys. Oceanogr.,* **6,** 238–242.

——, and J. S. Allen, 1976: Some three-dimensional characteristics of low-frequency current fluctuations near the Oregon coast. *J. Phys. Oceanogr.,* **6,** 181–199.

Martin, P. J., 1985: Simulation of the mixed layer at OWS November and Papa with several models. *J. Geophys. Res.*, **90,** 903–916.

Mellor, G. L., and T. Yamada, 1982: Development of a turbulence closure model for geophysical fluid problems. *Rev. Geophys. Space Phys.,* **20,** 851–875.

Moum, J. N., and J. D. Nash, 2000: Topographically induced drag

and mixing at a small bank on the continental shelf. *J. Phys. Oceanogr.,* **30,** 2049–2054.

Murphy, A. H., 1992: Climatology, persistence, and their linear combination as standards of reference in skill scores. *Wea. Forecasting,* **7,** 692–698.

——, 1995: The coefficients of correlation and determination as measures of performance in forecast verification. *Wea. Forecasting,* **10,** 681–688.

Nash, J. D., and J. N. Moum, 2001: Internal hydraulic flows on the continental shelf: High drag states over a small bank. *J. Geophys. Res.,* **106,** 4593–4611.

Oke, P. R., J. S. Allen, R. N. Miller, and G. D. Egbert, 2002a: A modeling study of the three-dimensional continental shelf circulation off Oregon. Part II: Dynamical analysis. *J. Phys. Oceanogr.,* **32,** 1383–1403.

——, ——, ——, ——, and P. M. Kosro, 2002b: Assimilation of surface velocity data into a primitive equation coastal ocean model. *J. Geophys. Res.,* in press.

Pickard, G. L., and W. J. Emery, 1990: *Descriptive Physical Oceanography: An Introduction.* Pergamon Press, 80 pp.

Samelson, R. M., and Coauthors, 2002: Wind stress forcing of the Oregon coastal ocean during the 1999 upwelling season. *J. Geophys. Res.,* in press.

Simonot, J., and H. Le Treut, 1986: A climatological field of mean optical properties of the world ocean. *J. Geophys. Res.,* **91,** 6642–6646.

Smagorinsky, J., 1963: General circulation experiments with primitive equations. I. The basic experiment. *Mon. Wea. Rev.,* **91,** 99–164.

Smith, R. L., 1974: A description of current, wind, and sea level variations during coastal upwelling off the Oregon coast, July-August 1972. *J. Geophys. Res.,* **79,** 435–443.

——, A. Huyer, and J. Fleischbein, 2001: The coastal ocean off Oregon from 1961 to 2000: Is there evidence of climate change or only of Los Niños? *Progress in Oceanography,* Vol. 49, Pergamon, 63–93.

Smolarkiewicz, P. K., 1984: A fully multidimensional positive definite advection transport algorithm with small implicit diffusion. *J. Comput. Phys.,* **54,** 325–362.

Stevenson, M. R., R. W. Garvine, and B. Wyatt, 1974: Lagrangian measurements in a coastal upwelling zone off Oregon. *J. Phys. Oceanogr.,* **4,** 321–336.